PHYSICAL REVIEW B **88**, 235207 (2013)

Second-harmonic generation spectroscopy of excitons in ZnO

M. Lafrentz,[1] D. Brunne,[1] A. V. Rodina,[2] V. V. Pavlov,[2] R. V. Pisarev,[2] D. R. Yakovlev,[1,2] A. Bakin,[3] and M. Bayer[1]
[1]*Experimentelle Physik 2, Technische Universität Dortmund, 44221 Dortmund, Germany*
[2]*Ioffe Physical-Technical Institute, Russian Academy of Sciences, 194021 St. Petersburg, Russia*
[3]*Institut für Halbleitertechnik, Technische Universität Braunschweig, 38106 Braunschweig, Germany*
(Received 6 August 2013; published 20 December 2013)

Nonlinear optics of semiconductors is an important field of fundamental and applied research, but surprisingly the role of excitons in the coherent processes leading to harmonics generation has remained essentially unexplored. Here we report results of a comprehensive experimental and theoretical study of the three-photon process of optical second-harmonic generation (SHG) involving the exciton resonances of the noncentrosymmetric hexagonal wide-band-gap semiconductor ZnO in the photon energy range of 3.2–3.5 eV. Resonant crystallographic SHG is observed for the $1s(A,B)$, $2s(A,B)$, $2p(A,B)$, and $1s(C)$ excitons. We show that SHG signals at these exciton resonances are induced by the application of a magnetic field when the incident and the SHG light wave vectors are along the crystal z axis where the crystallographic SHG response vanishes. A microscopic theory of SHG through excitons is developed, which shows that the nonlinear interaction of coherent light with excitons has to be considered beyond the electric-dipole approximation. Depending on the particular symmetry of the exciton states SHG can originate from the electric- and magnetic-field-induced perturbations of the excitons due to the Stark effect, the spin as well as orbital Zeeman effects, or the magneto-Stark effect. The importance of each mechanism is analyzed and discussed by confronting experimental data and theoretical results for the dependences of the SHG signals on photon energy, magnetic field, electric field, crystal temperature, and light polarization. Good agreement is obtained between experiment and theory proving the validity of our approach to the complex problem of nonlinear interaction of light with ZnO excitons. This general approach can be applied also to other semiconductors.

DOI: 10.1103/PhysRevB.88.235207 PACS number(s): 71.35.Ji, 42.65.Ky, 78.20.Ls

I. INTRODUCTION

Nonlinear optics has opened multifaceted possibilities for studying and tailoring light-matter interaction. Nowadays nonlinear optical phenomena and materials are a broad basis for fundamental and applied research.[1–5] In linear optics propagation, absorption, and emission of light are essentially single-photon processes. In contrast, in nonlinear optics the interaction of light with a medium is governed by multiphoton processes. Obviously the light-matter interaction becomes more intricate. Linear and nonlinear optical experiments address different types of optical susceptibilities, still they all are determined by the features of the crystal structure of the material under study as well as the resulting charge and spin properties. Therefore they open versatile opportunities for in-depth analysis from different perspectives. In this sense, linear and nonlinear optics may be regarded as complementary to each other in material investigations.

In nonlinear optics frequency conversion processes such as the second, third, and higher order harmonics generation as well as the sum and difference frequency generation play a particularly important role.[1–3] Among these phenomena, most prominent is the simplest three-photon process of optical second-harmonic generation (SHG). First, the parity selection rules for the optical transitions between the contributing electronic states radically differ from those in linear optics and also from other, more complicated nonlinear phenomena. Second, besides the parity selection rules, the time-reversal symmetry operation is a principally important factor in harmonics generation, when the spin system becomes involved in applied magnetic fields or in magnetically ordered materials.[6–8]

From the beginning of nonlinear optics, optical generation of second and higher order harmonics has been the subject of active research in various semiconductors.[9,10] However, the majority of these studies, typically performed on bulk crystals or thin films, were limited to fixed excitation wavelengths when the fundamental and harmonics photon frequencies were in the transparency region, below the fundamental band gap. This approach is motivated by avoiding any absorption in the medium which would impede potential applications. There are only a few examples where the SHG spectroscopic studies of semiconductors cover broad spectral ranges. Absolute values of the SHG coefficients for bulk zinc-blende ZnTe, ZnSe, and ZnS were measured at room temperature in the SHG spectral range of 1.8–4.8 eV.[11] Spectroscopic SHG in bulk GaAs was reported in the range of 2–5 eV, covering several electronic transitions at critical points.[12] The SHG spectral features found for these materials were in reasonable agreement with theoretical calculations and experimental data acquired by other techniques. For hexagonal ZnO, the material selected for the present study, SHG was reported for selected wavelengths below the band gap in numerous publications, see, e.g., Refs. 13–16. Furthermore, also spectroscopic SHG studies in the range 2.25–3.44 eV were reported for ZnO microcrystallite thin films.[17] The SHG output was found to increase significantly in the vicinity of the direct band gap. SHG over broad infrared spectral ranges was also applied to various chalcopyrites and semiconductors of practical importance, see, e.g., Refs. 18 and 19 and references therein.

In semiconductors the optical properties in close vicinity to the band gap are largely determined by excitons, bound complexes of an electron and a hole. The exciton energy levels including their spin properties have been intensely studied using both linear and nonlinear optical methods such as absorption, reflection, photoluminescence, two-photon absorption, four-wave mixing, etc.[9,10] Surprisingly, the contributions of excitons to harmonics generation have remained essentially unexplored. Typically studies lack a microscopic theoretical explanation, with scarce exceptions.[20–22] Experimental observations were reported for forbidden SHG in resonance with the $2p$ Wannier exciton in ZnSe thin films;[23,24] resonant SHG at the $1s$ orthoexciton in Cu_2O;[25,26] and second- and third-harmonic spectroscopy of excitons in a homoepitaxial GaN layer.[27] An early attempt to detect SHG signals in the spectral region of the C exciton in ZnO and the $1s$ excitons in CuCl was undertaken in Refs. 28 and 29. The concept of Wannier excitons was used in the SHG study of CuCl, whereas Frenkel excitons were explored in SHG studies of a C_{60} molecular crystal.[30,31]

Detail insight into the role of excitons in harmonics generation can be taken if the studies are performed at low temperatures with a high spectral resolution. External magnetic and electric fields can perturb and mix charge and spin states, providing novel mechanisms for nonlinear harmonics generation. For example, in diamagnetic materials GaAs and CdTe the orbital quantization is the origin of magnetic-field-induced SHG.[32,33] In diluted magnetic semiconductor (Cd,Mn)Te, on the other hand, the giant Zeeman spin splitting was shown to be the source of magnetic-field-induced SHG.[34] Even for the centrosymmetric magnetic semiconductors EuTe and EuSe a magnetic field was found to induce SHG with high efficiency.[35,36]

This rudimentary state of the exciton SHG problem has motivated our spectroscopic research of SHG as the simplest frequency conversion process in the wide-band-gap semiconductor ZnO, characterized by a large exciton binding energy of 60 meV and a rich exciton level structure.[37] This material has recently gained substantial renewed interest, partly because the large exciton binding energy could lead to lasing by exciton recombination even at room temperature. This and other potential ZnO applications are discussed in the comprehensive review by Özgür *et al.*[38] In order to get deeper insight, our study of SHG at excitons is performed in applied magnetic and electric fields. In conjunction with a detailed theoretical analysis we show that SHG spectroscopy allows us to work out the underlying microscopic mechanisms of the nonlinear process of simultaneous coherent two-photon excitation and subsequent one-photon emission involving excitons. Magnetic and electric fields can perturb the exciton states through the Stark, the magneto-Stark, and the Zeeman effects and may act therefore as sources of SHG carrying characteristic signatures for the chosen field geometry. Our findings open new opportunities for studying exciton complexes in detail and involving them in frequency conversion processes.

The paper is organized as follows. In Sec. II we describe the crystallographic and electronic structures as well as the optical and magneto-optical properties of hexagonal ZnO. Also a symmetry analysis of the SHG polarization selection rules is given. Experimental details are presented in Sec. III, followed by Sec. IV where the experimental data are described. In Sec. V the microscopic theory of the SHG is introduced and several mechanisms involving exciton states are suggested. The comparison of experiment and theory in Sec. VI allows assignment of particular SHG signals to the specific mechanisms.

II. SECOND-HARMONIC GENERATION IN ZnO

A. Symmetry of electronic states, excitons, and polaritons

ZnO crystallizes preferably in the wurtzite-type structure,[38,39] see Fig. 1(a), characterized by two interconnected sublattices of Zn^{2+} and O^{2-} ions with a strong ionic binding. The lattice constants of ZnO are $a_0 = 3.2495$ Å and $c_0 = 5.2069$ Å.[40] The unit cell is formed by two Zn^{2+} and two O^{2-} ions ($Z = 2$) each of them being tetrahedrally surrounded by four ions of the other species. Wurtzite ZnO has a hexagonal crystal lattice, belonging to the point group $6mm$ and space group $P6_3mc$.[41,42] The z direction of the used Cartesian xyz system is chosen parallel to the polar hexagonal [0001] axis, the so-called c axis, which subsequently will be referred to as z axis following the Birss notation $[0001] \parallel \mathbf{z}$ and $[1\bar{1}00] \parallel \mathbf{y}$.[43] From the optical point of view ZnO is a uniaxial material with the optical axis directed along the crystallographic z axis.

The electronic band structure of wurtzite ZnO is shown in Fig. 1(b). The valence band is formed by the $2p$ orbitals of the O^{2-} ions and the conduction band is formed by the $4s$ orbitals of the Zn^{2+} ions. The $2p$ orbitals are split by the hexagonal crystal field into two Γ_5 and Γ_1 subbands. Including the spin through the spin-orbit interaction leads to a further splitting into three twofold degenerate valence band states $(\Gamma_1 \oplus \Gamma_5) \oplus \Gamma_7 = \Gamma_7 \oplus \Gamma_9 \oplus \Gamma_7$. In all wurtzite-type semiconductors these bands are usually labeled from higher to lower energies as A (Γ_9), B (Γ_7), and C (Γ_7) bands. However, ZnO has an inverted valence band ordering A (Γ_7), B (Γ_9), and C (Γ_7).[37] The selection rules for transitions from the upper valence bands A (Γ_7) and B (Γ_9) to the conduction band (Γ_7) are essentially the same, because the admixture of the $|z\rangle$ character to the Bloch wave functions of the A (Γ_7) valence band is small.[44] As a result, these transitions are allowed for $\mathbf{E}^\omega \perp \mathbf{z}$, where $\mathbf{E}^\omega$ is

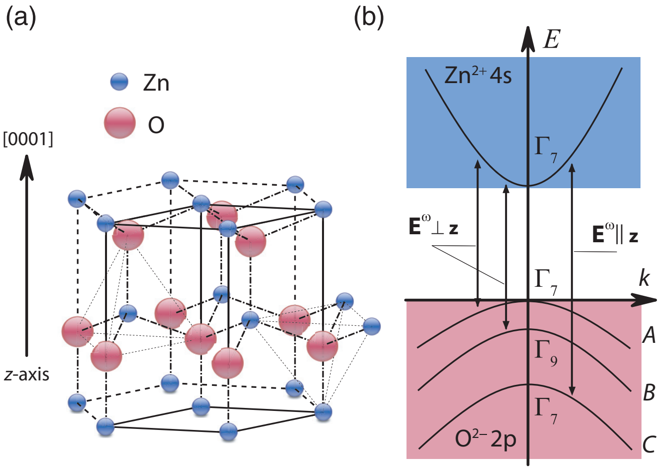

FIG. 1. (Color online) (a) Uniaxial crystal structure of wurtzite ZnO, $[0001] \parallel \mathbf{z}$ is the hexagonal crystallographic axis. (b) Electronic band structure of wurtzite ZnO. The hexagonal crystal field is responsible for the energy splitting between the A, B, and C valence bands.

the electric field of the fundamental light wave. Transitions from the C (Γ_7) valence band to the conduction band (Γ_7) are allowed for $\mathbf{E}^{\omega} \parallel \mathbf{z}$.

Correspondingly, three exciton series are formed in ZnO by a Γ_7 electron and a hole from one of the A (Γ_7), B (Γ_9), or C (Γ_7) valence bands. These excitons have approximately the same binding energy of $\simeq$60 meV and a Bohr radius of $\simeq$1.8 nm. The exciton symmetry results from the direct product of the envelope function symmetry and the symmetry of conduction and valence band Bloch states, see e.g., Refs. 45 and 46. The energies of the resulting exciton states are split by the short-range exchange interaction. For the s-symmetry excitons of the A and B series, the strongest state has Γ_5 symmetry. It is twofold degenerate and polarized perpendicular to the z axis, while for the C exciton it has Γ_1 symmetry and is polarized parallel to the z axis. As a result, for light propagating along the z axis ($\mathbf{k} \parallel \mathbf{z}$) both Γ_5 excitons are transversal, while the Γ_1 exciton is longitudinal and cannot be excited. For light with $\mathbf{k} \perp \mathbf{z}$, one of the Γ_5 exciton states is transversal and the other is longitudinal, while the Γ_1 exciton is transversal. The resonances of the longitudinal excitons are shifted to higher energies by the long-range exchange interaction.

The strong light-matter interaction in ZnO leads to the formation of exciton-polaritons and their symmetries depend on the direction of the light propagation. The interaction of the transversal excitons with photons leads to the formation of two transversal, lower and upper polariton branches (LPB and UPB). Their dispersion relations can be obtained from the condition $\varepsilon_{\perp}(\omega,\mathbf{k}) = (kc/\omega)^2$ for the Γ_5 excitons and $\varepsilon_{\parallel}(\omega,\mathbf{k}) = (kc/\omega)^2$ for the Γ_1 excitons. Here c is the speed of light and ω is the photon frequency. $\varepsilon_{\perp}$ and $\varepsilon_{\parallel}$ are the dielectric functions for the electric field of light polarized perpendicular and parallel to the z axis, respectively, including contributions of exciton resonances with energies close to $\hbar\omega$. The energies of the UPB at $k = 0$ coincide with the energies of the longitudinal excitons determined from $\varepsilon_{\perp,\parallel}(\omega,k = 0) = 0$, while the energies of the LPB at $k \to \infty$ coincide with the energies of the transversal excitons. If $\mathbf{k}$ is not parallel or perpendicular to the crystal z axis, one obtains the so called mixed-mode polaritons.[47–49]

B. Polarization selection rules for SHG

Wurtzite ZnO belongs to the noncentrosymmetric point group $6mm$ and, consequently, the leading-order SHG is allowed in the electric-dipole (ED) approximation. The crystallographic SHG polarization $P^{2\omega}$ can be written as

$$P_i^{2\omega} = \epsilon_0 \chi_{ijl}^{\text{cryst}}(-2\omega;\omega,\omega) E_j^{\omega} E_l^{\omega}, \tag{1}$$

where i,j,l are the Cartesian indices, ϵ_0 is the vacuum permittivity, $\chi_{ijl}^{\text{cryst}}$ is the nonlinear optical susceptibility, and $E_{j(l)}^{\omega}$ are the components of the fundamental light electric field $\mathbf{E}^{\omega}$. In the ED approximation and in the absence of external fields a group theoretical analysis predicts the following nonzero components of the crystallographic nonlinear optical susceptibility for bulk ZnO $\chi_{ijl}^{\text{cryst}}$: $\chi_{xxz} = \chi_{xzx} = \chi_{yyz} = \chi_{yzy}$, $\chi_{zxx} = \chi_{zyy}$, and χ_{zzz}.[3,50]

Note that Eq. (1) accounts only for the ED contributions on or off resonant with electronic band transitions at the fundamental and SHG photon frequencies ω and 2ω, respectively. However, more generally the SHG process can involve also electric-quadrupole (EQ) and magnetic-dipole (MD) contributions. They become important when the outgoing SHG is resonant with the exciton energy $\mathcal{E}_{\text{exc}}$, for example. Taking into account higher order contributions and the feasibility of a resonance, the incoming fundamental electric field $\mathbf{E}^{\omega}(\mathbf{r},t) = \mathbf{E}^{\omega} \exp[\mathrm{i}(\mathbf{kr} - \omega t)]$ generates an effective polarization inside the semiconductor at the double frequency as[51]

$$P_{\text{eff},i}^{2\omega}(\mathcal{E}_{\text{exc}}) = \epsilon_0 \chi_{ijl}^{\text{cryst}}(\mathcal{E}_{\text{exc}},\mathbf{k}_{\text{exc}}) E_j^{\omega} E_l^{\omega}, \tag{2}$$

where the nonlinear optical susceptibility $\chi_{ijl}^{\text{cryst}}(\mathcal{E}_{\text{exc}},\mathbf{k}_{\text{exc}})$ describes the spatial-dispersion phenomena entering in the EQ and MD approximations. $\mathbf{k}_{\text{exc}} = 2n\mathbf{k}$ is the exciton wave vector, n is the refractive index at the fundamental energy $\hbar\omega$, and $\mathbf{k}$ is the wave vector of the incoming light.

Additional information on the exciton energy levels including their spin structure, as well as on their wave functions can be obtained by applying external fields. The symmetries of exciton states may be modified by electric or magnetic fields, enabling mixing of states. This opens the way for novel SHG mechanisms induced by the fields. In this case, the effective polarization inside the semiconductor can be written as

$$P_{\text{eff,B,E},i}^{2\omega}(\mathcal{E}_{\text{exc}}) = \epsilon_0 \chi_{ijl}(\mathcal{E}_{\text{exc}},\mathbf{k}_{\text{exc}},\mathbf{B},\mathbf{E}) E_j^{\omega} E_l^{\omega}, \tag{3}$$

where the nonlinear optical susceptibility $\chi_{ijl}(\mathcal{E}_{\text{exc}},\mathbf{k}_{\text{exc}},\mathbf{B},\mathbf{E})$ accounts for phenomena induced by the external magnetic ($\mathbf{B}$) and electric ($\mathbf{E}$) fields. The nonlinear polarizations in Eqs. (1)–(3) are the sources of the outgoing SHG electric field $\mathbf{E}^{2\omega}(\mathbf{r},t) \propto \mathbf{P}^{2\omega} \exp[\mathrm{i}(2\mathbf{kr} - 2\omega t)]$ with SHG intensity $I^{2\omega} \propto |\mathbf{P}^{2\omega}|^2$.

For a resonant SHG process, which involves the ground state of the unexcited crystal $|G\rangle$ and an exciton state $|\text{Exc}\rangle$, the optical transition from $|G\rangle$ to $|\text{Exc}\rangle$ should be allowed both for the two-photon excitation and the one-photon emission processes. Fulfillment of this condition strongly depends on the crystal symmetry and experimental geometry. With including excitonic effects, this situation becomes richer due to the different symmetries of the exciton states with s, p, and d type of envelope wave functions.

Furthermore, external perturbations such as stress, electric, or magnetic field can mix the exciton states, thereby reducing their symmetry. For linear optical spectroscopy on ZnO (e.g., one-photon absorption or emission) only s exciton states are active, while p states cannot be seen. In order to study p exciton states, either nonlinear spectroscopy (e.g., two-photon absorption) or external perturbations, which mix s and p states have to be used. To study exciton states and their mixing, we performed detailed experimental and theoretical studies of ZnO, serving as a model system, by SHG spectroscopy with application of magnetic and electric fields.

III. EXPERIMENT

A hydrothermally grown hexagonal ZnO crystal of high optical quality with [0001] orientation and thickness of 500 μm was chosen for this study. The SHG technique used for exciton spectroscopy was described in Ref. 33. The linearly polarized

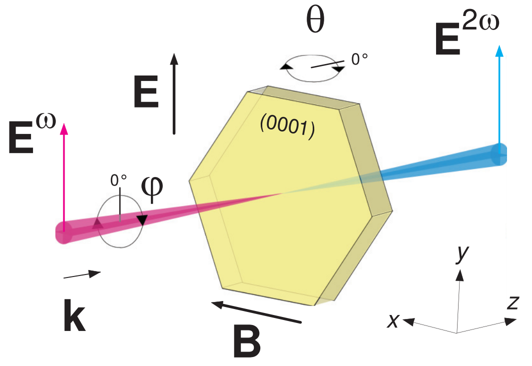

FIG. 2. (Color online) Sketch demonstrating the measurement geometry. θ is the sample tilting angle and φ is the turning angle of $\mathbf{E}^{\omega(2\omega)}$ around $\mathbf{k}$. Electric and magnetic fields are perpendicular to each other and to the propagation direction of the light $\mathbf{E} \perp \mathbf{B} \perp \mathbf{k}$.

fundamental light with photon energy $\hbar\omega$ was provided by a laser system with an optical parametric oscillator tunable in the spectral range of interest ($\hbar\omega = 1.6$–1.75 eV) and generating optical pulses of 7 ns duration with energies up to 3 mJ per pulse. The experiments were performed in the transmission geometry with the light wave vector $\mathbf{k}$ either parallel or tilted to the z axis of the ZnO sample. The SHG signal at photon energies $2\hbar\omega$ was spectrally selected by a monochromator and detected by a cooled charge-coupled-device camera. The experimental geometry is shown in Fig. 2. Here θ is the angle between the light wave vector $\mathbf{k}$ and the z axis which gives the sample tilting. φ is the azimuthal angle of the fundamental light polarization, where $\varphi = 0^\circ$ coincides with the crystallographic y axis. Magnetic fields $\mathbf{B}$ up to 10 T generated by a split-coil superconducting solenoid were applied in the Voigt geometry ($\mathbf{B} \perp \mathbf{k}$) or the Faraday geometry ($\mathbf{B} \parallel \mathbf{k}$). External electric fields $\mathbf{E}$ up to 550 V/cm were applied via contacts perpendicular both to the magnetic field and the propagation direction of the light $\mathbf{E} \perp \mathbf{B} \perp \mathbf{k}$. The sample temperature T was varied in the range 1.6–125 K.

As we will show below in Secs. IV and V, decisive experiments for distinguishing different microscopic contributions to the SHG signal are measurements of the rotational anisotropy, i.e., the dependence of the SHG signal on the azimuthal angle φ. Such rotational anisotropies were measured for four different geometries.

(1) $I_{\parallel}^{2\omega} \mapsto \mathbf{E}^{2\omega} \parallel \mathbf{E}^{\omega}$, fundamental and SHG light polarizations are rotated synchronously, such that they are parallel to each other.

(2) $I_{\perp}^{2\omega} \mapsto \mathbf{E}^{2\omega} \perp \mathbf{E}^{\omega}$, fundamental and SHG light polarization are rotated synchronously, such that the SHG light polarization is perpendicular to the fundamental light.

(3) $I_{\parallel\mathbf{B}}^{2\omega} \mapsto \mathbf{E}^{2\omega} \parallel \mathbf{B}$, SHG light polarization is fixed parallel to the magnetic-field direction, while the fundamental light polarization is rotated around $\mathbf{k}$.

(4) $I_{\perp\mathbf{B}}^{2\omega} \mapsto \mathbf{E}^{2\omega} \perp \mathbf{B}$, SHG light polarization is fixed perpendicular to the magnetic-field direction, while the fundamental light polarization is rotated around $\mathbf{k}$.

The corresponding patterns of rotational anisotropies are modeled according to Eqs. (1)–(3). The results are discussed in Sec. VI.

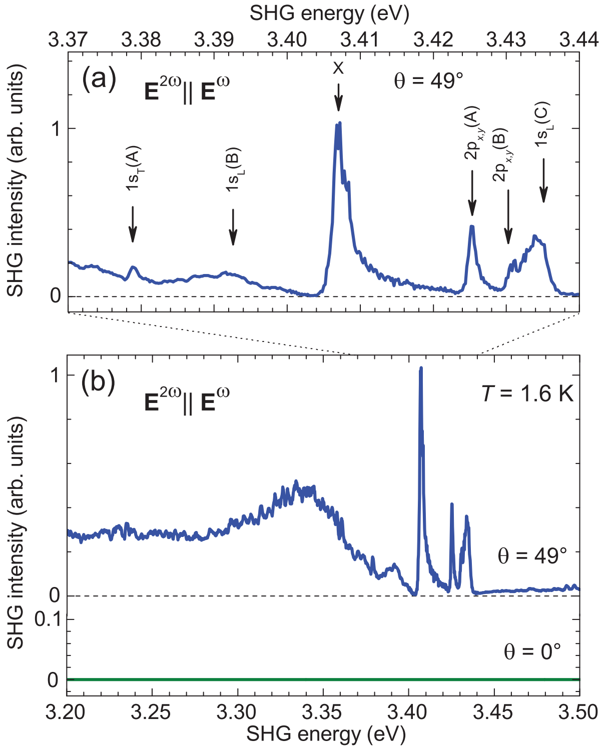

FIG. 3. (Color online) Crystallographic SHG spectra of ZnO for $\mathbf{E}^{2\omega} \parallel \mathbf{E}^{\omega}$ and $\varphi = 90^\circ$ (compare with anisotropies in Fig. 4), measured at $T = 1.6$ K. (a) Close-up of the exciton spectral range 3.37–3.44 eV for $\theta = 49^\circ$. (b) Extended spectral range 3.2–3.5 eV for $\theta = 49^\circ$ and 0°. SHG signals vanish for $\mathbf{k} \parallel \mathbf{z}$ ($\theta = 0^\circ$).

IV. EXPERIMENTAL RESULTS

A. Crystallographic SHG

It follows from the symmetry analysis of the selection rules in Sec. II B that for laser light propagating along the hexagonal z axis ($\mathbf{k} \parallel \mathbf{z}$) no ED crystallographic SHG is allowed. This geometry addresses solely components of the susceptibility without z index, which are all zero. Indeed, no SHG signals are found experimentally in the vicinity of the ZnO band gap for zero tilting angle $\theta = 0^\circ$, see Fig. 3(b).

For tilted geometry, $\mathbf{k}\angle\mathbf{z} \neq 0$, SHG is provided by the nonzero $\chi_{ijl}^{\mathrm{cryst}}$ components with z index, see Eq. (1). For parallel orientation of the linear polarizations of fundamental and SHG light ($\mathbf{E}^{2\omega} \parallel \mathbf{E}^{\omega}$), strong SHG signals are found for $\varphi = 90^\circ$ (see Fig. 4). As one can see in Fig. 3(b), the SHG consists of a broad band in the spectral range below the exciton transitions. Furthermore, several sharp lines show up in the exciton spectral range. Above the band gap the SHG signal vanishes. The SHG intensity shows pronounced rotational anisotropies summarized in Fig. 4. These anisotropies allow distinguishing of the SHG signals from two-photon photoluminescence signals which are expected to be isotropic.

The exciton spectral range is shown in more detail in Fig. 3(a). Arrows mark the reported energies of the different exciton states in hexagonal ZnO.[52] Letters T and L mark the transversal and longitudinal excitons, respectively. A feature at 3.407 eV has not been reported in literature so far. It will be referred to as the X line and discussed in more detail in Sec. VI. In the tilted geometry, both s and p exciton states are

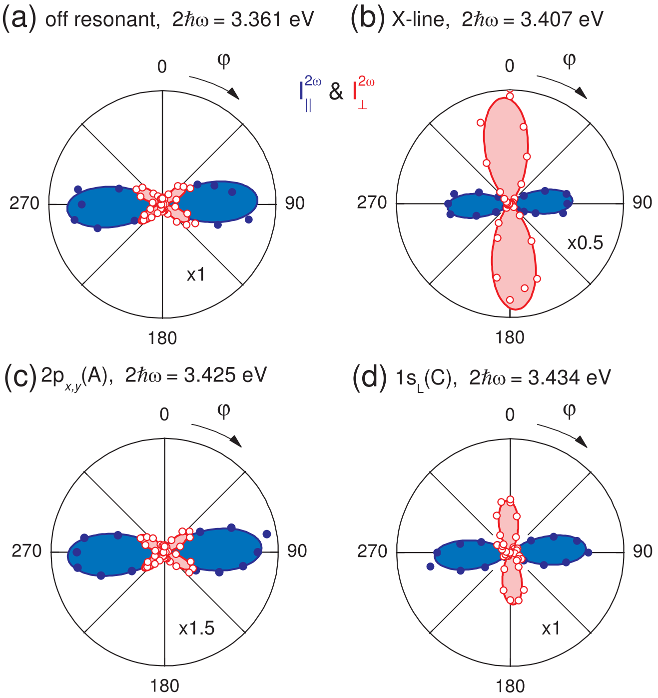

FIG. 4. (Color online) Angular dependences of the crystallographic SHG measured at $\theta = 49^\circ$ for different energies. Filled (blue) and open (red) circles represent the geometries $\mathbf{E}^{2\omega} \parallel \mathbf{E}^{\omega}$ and $\mathbf{E}^{2\omega} \perp \mathbf{E}^{\omega}$, respectively. Lines and shaded areas show best fits according to Eq. (1). (a) Off-resonant signal at $2\hbar\omega = 3.361$ eV. (b) Unidentified X line at $2\hbar\omega = 3.407$ eV. Signal is scaled down by a factor of 2. (c) $2p(A)$ exciton line at $2\hbar\omega = 3.425$ eV. Signal is scaled up by a factor of 1.5. (d) $1s_{\mathrm{L}}(\mathrm{C})$ exciton line at $2\hbar\omega = 3.434$ eV.

SHG active. Using linear spectroscopy, only the $1s$ exciton states are observed in absorption and reflection spectra due to their strong oscillator strength. By contrast, the SHG intensity in the range of $1s$ states of A and B excitons is surprisingly much weaker than the intensity of their excited $2s$ and $2p$ states. This observation is a clear manifestation that nonlinear SHG spectroscopy addresses exciton properties inaccessible by linear spectroscopy.

Rotational anisotropy diagrams were measured for $\mathbf{E}^{2\omega} \parallel \mathbf{E}^{\omega}$ and $\mathbf{E}^{2\omega} \perp \mathbf{E}^{\omega}$ at the following photon energies: 3.361, 3.379, 3.391, 3.400, 3.407, 3.413, 3.425, 3.430, 3.434, and 3.444 eV. Those anisotropies in Figs. 4(a) and 4(c) are representative for the off-resonant and A,B exciton regions. Figures 4(b) and 4(d) show rotational anisotropies specific for energies close to the X line and the $1s_{\mathrm{L}}(C)$ exciton. The strongest signal for $\mathbf{E}^{2\omega} \parallel \mathbf{E}^{\omega}$ is found for all energies in the (yz) plane meaning that the shape is dominated by the χ_{zzz} component. Indeed, the fitting procedure gives an χ_{zzz} value which is an order of magnitude larger than the other components. For the crossed geometry $\mathbf{E}^{2\omega} \perp \mathbf{E}^{\omega}$, the fitting procedure gives the same ratio of nonlinear components. On the other hand, for energies close to the X line and the $1s_{\mathrm{L}}(C)$ exciton in Figs. 4(b) and 4(d), the SHG intensity $I_{\perp}^{2\omega}$ has a pronounced feature along the y axis, which can be explained by a phase shift. The real and imaginary parts of the nonlinear components change signs in these specific regions, leading to a strong distortion in the crossed geometry $\mathbf{E}^{2\omega} \perp \mathbf{E}^{\omega}$.

We note that our experiments do not allow us to measure the absolute values of the nonlinear susceptibilities. Therefore, it is difficult to compare the relative nonlinearities for SHG signals which are widely separated on the photon energy scale. To measure the absolute values of the nonlinear susceptibilities one has to take into account the complex linear refraction indices for both the fundamental and the SHG photon energies.[29] We also note that the expected quadratic increase of the SHG intensity with the fundamental power has been confirmed for the off-resonant and on-resonant crystallographic SHG signals, as well as for the magnetic-field-induced SHG signals, described in the next subsection.

B. Magnetic-field-induced SHG

For investigating magnetic-field-induced SHG we chose the experimental geometry with $\theta = 0^\circ$, where the crystallographic SHG signal vanishes. A magnetic field $B = 5$ T was applied perpendicular to the z axis in the geometry $\mathbf{B} \perp \mathbf{k} \parallel \mathbf{z}$. SHG signals are observed only in resonance with excitons, see Fig. 5. Two strong lines are seen in the spectral range of the $2s/2p(A,B)$ exciton states and three much weaker lines in the range of the $1s(A,B)$ excitons. Note that this behavior differs from the observations in GaAs and CdTe, where the $1s$ exciton line always dominates in the magnetic-field-induced SHG spectrum.[32,33] In ZnO, the weak SHG intensity observed at the $1s(A,B)$ excitons can be related to the strong absorption of SHG light due to the large absolute values of the complex dielectric function.[53]

A magnetic field is an axial vector of even parity and, therefore, it is not supposed to mix wave functions of opposite parities. In spite of this restriction, a strong magnetic-field-induced contribution to SHG was found in ZnO. An in-depth

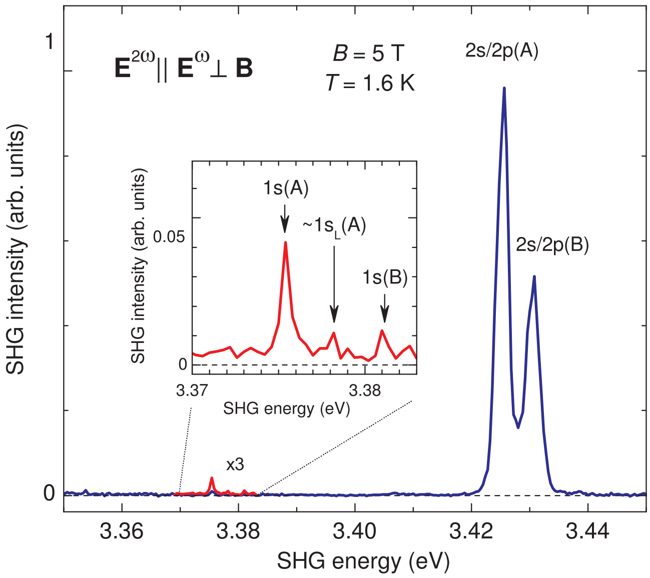

FIG. 5. (Color online) Magnetic-field-induced SHG spectrum of ZnO in a wide energy range 3.35–3.45 eV for $\mathbf{E}^{2\omega} \parallel \mathbf{E}^{\omega} \perp \mathbf{B}$, $\theta = 0^\circ$ and $\varphi = 0^\circ$ at $T = 1.6$ K. Inset shows the $1s$ exciton region zoomed by a factor of 20. The integration time for recording the data shown by the red line was tripled compared to the data shown by the blue line.

analysis of the SHG microscopic mechanisms is required for understanding these experimental findings. Such analysis based on the theoretical model of Sec. V will be given in Sec. VI.

1. SHG on $1s(A,B)$ excitons

Let us consider the experimental observations in the $1s$ exciton region in magnetic field more thoroughly. The corresponding SHG spectra for different fields up to 10 T are shown in Fig. 6(a). Three lines corresponding to the $1s(A)$ transversal and longitudinal polaritons[54] and $1s(B)$ transversal polariton are clearly seen at the strongest field with the first line at 3.3754 eV being the most intense. The integrated intensity of the $1s_T(A,\Gamma_5/\Gamma_1)$ line shows a B^2 dependence, see Fig. 7(a). Its temperature dependence measured at $B = 7$ T shows a rapid decrease; see Fig. 14(a). For excitons with strong binding energies it is expected that the diamagnetic shift of their $1s$ states for the magnetic-field strengths used here is very small, as illustrated in Fig. 6(b).

Figure 6(c) shows the rotational anisotropies of the SHG intensities in a magnetic field of 5 T for the parallel $\mathbf{E}^{2\omega} \parallel \mathbf{E}^{\omega}$ and the perpendicular $\mathbf{E}^{2\omega} \perp \mathbf{E}^{\omega}$ detection geometries for the $1s_T(A,\Gamma_5/\Gamma_1)$ exciton. The rotational anisotropies show twofold symmetry patterns, have the same amplitudes, and are rotated relative to each other by 90°, where the strongest signal is found for $\varphi = 0^\circ$ in the parallel geometry. These patterns clearly differ from the crystallographic ones in Fig. 4, highlighting the difference of involved SHG mechanisms. The fits are done according to Eqs. (9) and (11) in Sec. V.

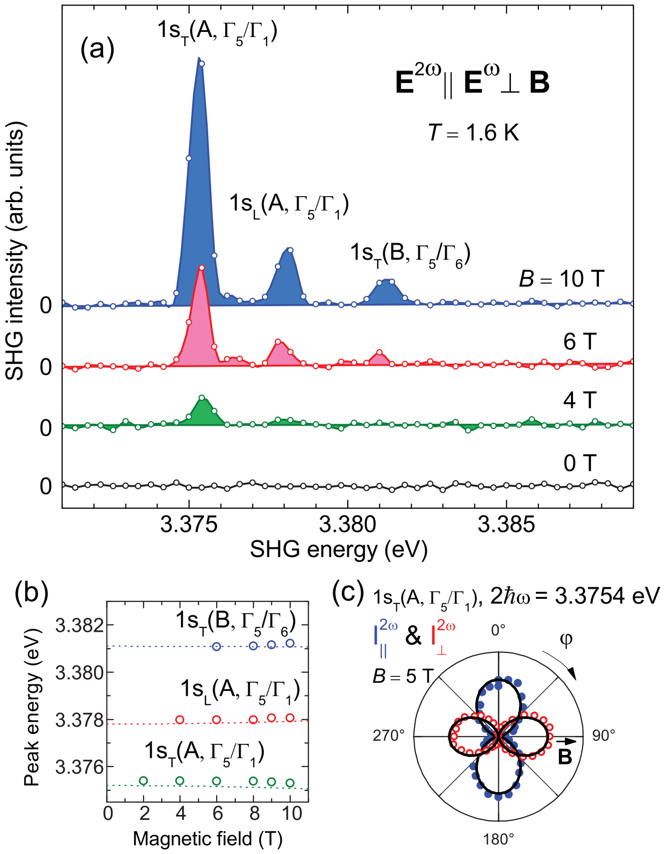

FIG. 6. (Color online) (a) Magnetic-field-induced SHG spectra in the range of the $1s(A,B)$ excitons in ZnO. (b) Magnetic-field dependence of the peak energy of the SHG exciton lines from (a), dashed lines are calculated after Eq. (A8). (c) Rotational anisotropy of SHG intensity measured for the strongest line at $B = 5$ T, detected for synchronous rotation of the linear polarizers for fundamental and SHG light: blue filled circles for $\mathbf{E}^{2\omega} \parallel \mathbf{E}^{\omega}$ and red open circles for $\mathbf{E}^{2\omega} \perp \mathbf{E}^{\omega}$. Black lines give best fits after Eqs. (9) and (11).

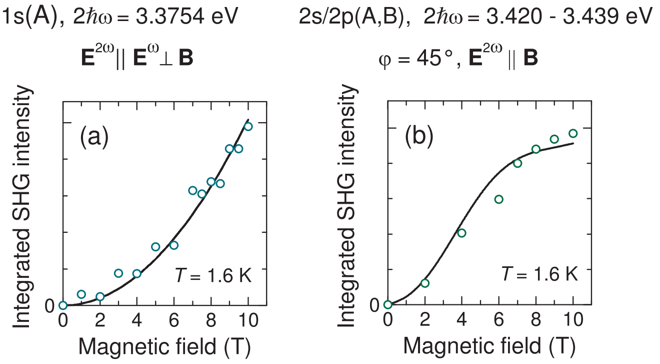

FIG. 7. (Color online) (a) Integrated SHG intensity for the strongest $1s$ line at $2\hbar\omega = 3.3754$ eV [compare Fig. 6(a)] as function of magnetic field (symbols). Line is the best fit with $I_{\parallel}^{2\omega} \propto B^2$. (b) Integrated SHG intensity in the spectral range of the $2s/2p(A,B)$ excitons at $2\hbar\omega = 3.420$–3.439 eV (compare Fig. 8) as function of magnetic field (symbols). Line gives model calculation for $2\hbar\omega = 3.4254$ eV (the energy of the strongest peak in the SHG spectra) and $\Gamma^i = 1.2$ meV.

2. SHG at $2s/2p(A,B)$ excitons

Figure 8(a) shows the magnetic-field-induced SHG spectra at the $2s/2p(A,B)$ exciton photon energies. A double peak structure with lines at 3.425 and 3.431 eV appears with increasing magnetic field, corresponding to the energies of the $2p(A,B)$ excitons.[55,56] In strong magnetic fields exceeding 7 T the doublet structure splits further into at least four peaks. In fact, more states can be distinguished in high magnetic fields when the signals in different polarization geometries are analyzed, see Fig. 8(b). The energy shifts of these lines are plotted as a fan chart diagram in Fig. 9, where the SHG peak intensities are represented by the symbol sizes. Here experimental results are compared with model calculations, which details are discussed below in Sec. VI B.

The magnetic-field dependence of the integrated SHG intensity of the $2s/2p$ states shows a quadratic increase at low fields $B < 6$ T, similar to the $1s$ exciton, and then tends to saturate for $B > 6$ T, see Fig. 7(b). This behavior, which was not observed for the $1s$ states, gives a strong indication that the mechanisms responsible for the magnetic-field-induced SHG differ for the $1s$ and the $2s/2p$ excitons in ZnO. The temperature dependence of the $2s/2p$ SHG intensity in Fig. 14(a) shows a similar but slightly faster decrease than that of the $1s$ excitons.

SHG rotational anisotropies detected in different geometries at $B = 10$ T for the $2s/2p(A,B)$ states are shown in Figs. 10 and 11. They have different patterns depending on the exciton state involved, see, e.g., Figs. 11(d) and 11(f). The anisotropies differ strongly in the amplitude ratios for different geometries. In the perpendicular geometry $\mathbf{E}^{2\omega} \perp \mathbf{E}^{\omega}$

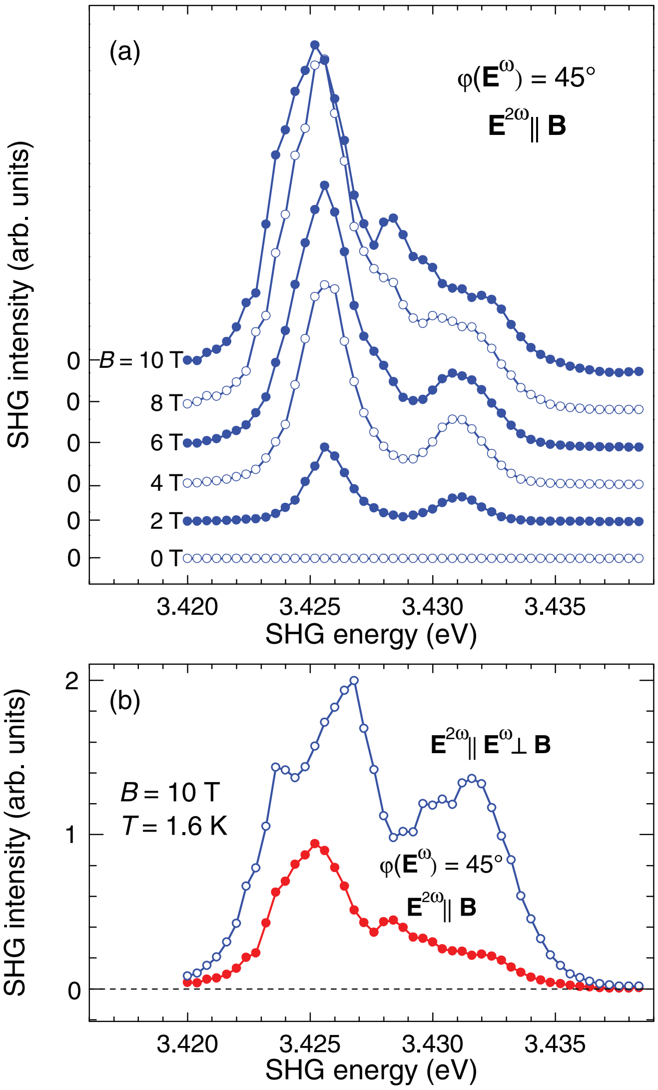

FIG. 8. (Color online) Magnetic-field-induced SHG spectra in the energy range of the $2s/2p$ exciton states measured at $T = 1.6$ K. (a) SHG spectra in different magnetic fields for $\mathbf{E}^{2\omega} \parallel \mathbf{B}$ and $\varphi(\mathbf{E}^{\omega}) = 45^\circ$. (b) SHG spectra at $B = 10$ T for $\mathbf{E}^{2\omega} \parallel \mathbf{E}^{\omega} \perp \mathbf{B}$ and $\mathbf{E}^{2\omega} \parallel \mathbf{B}$ with $\varphi(\mathbf{E}^{\omega}) = 45^\circ$.

the shapes are quite different, compare Figs. 11(b) and 11(f), leading to the assumption that the responsible SHG mechanisms are different and vary with the photon energy.

3. Magnetic-field-induced versus crystallographic SHG

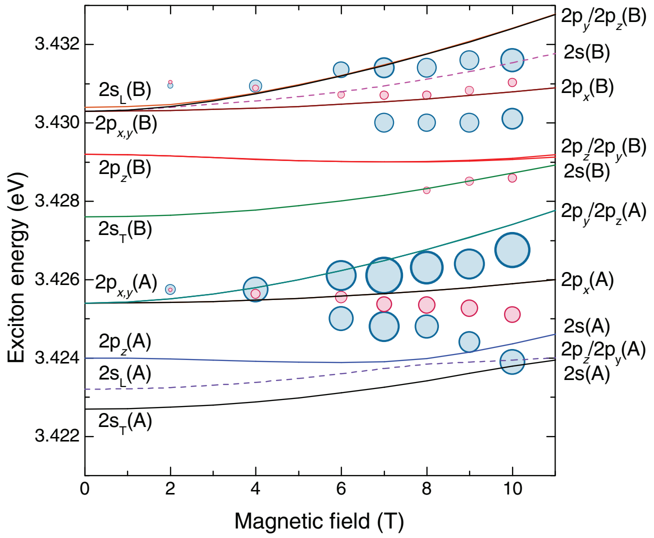

FIG. 9. (Color online) Fan chart diagram for the magnetic-field dependences of the $2s$ and $2p$ excited state energies of the A and B excitons. Symbols are experimental data with their size scaled by the observed peak intensity. Blue and red circles are observed in the geometries $\mathbf{E}^{2\omega} \parallel \mathbf{E}^{\omega} \perp \mathbf{B}$ and $\mathbf{E}^{2\omega} \parallel \mathbf{B}$ with $\varphi(\mathbf{E}^{\omega}) = 45^\circ$, respectively. Solid lines give the energies of the coupled $2s/2p_z/2p_y$ and the $2p_x$ states according to the calculations in the Appendix and after Eq. (A12). Labels at low fields indicate the zero field exciton energies, while labels at high fields give the dominant component in the mixed exciton wave functions.

It is instructive to compare the intensities of the crystallographic and the magnetic-field-induced SHG signals. This comparison is presented in Fig. 12, where all four panels, recorded with the tilting angle $\theta \approx 45^\circ$, have the same intensity scale. In absence of magnetic field the strongest crystallographic SHG signal is found for $\mathbf{E}^{2\omega} \parallel \mathbf{E}^{\omega}$ and $\varphi(\mathbf{E}^{\omega}) = 90^\circ$, while it vanishes for $\mathbf{E}^{2\omega} \parallel \mathbf{E}^{\omega}$ and $\varphi(\mathbf{E}^{\omega}) = 0^\circ$; see Fig. 4(c). Figure 12(a) demonstrates that even for a tilted sample no signal is observed for $\mathbf{E}^{2\omega} \parallel \mathbf{E}^{\omega}$, $\varphi(\mathbf{E}^{\omega}) = 0^\circ$. Thus, for a tilted sample Fig. 12(b) shows the intensity of a pure magnetic-field-induced SHG signal for the $2s/2p(A,B)$ states, which is even more intense than the strongest crystallographic signal $I_{\perp}^{2\omega}$ in Fig. 12(c) observed for the $1s_{\mathrm{L}}(C)$ with $\mathbf{E}^{2\omega} \perp \mathbf{E}^{\omega}$ and $\varphi(\mathbf{E}^{\omega}) = 0^\circ$, see Fig. 4(c). Consequently, we can conclude that the susceptibilities of magnetic-field-induced

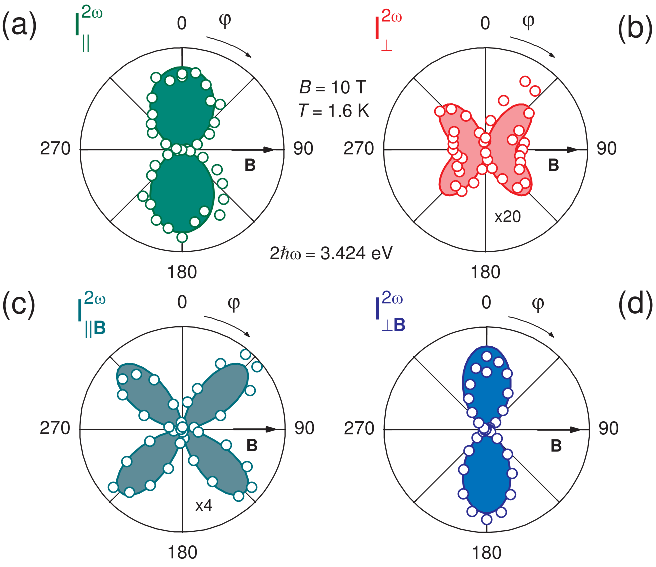

FIG. 10. (Color online) Angular dependences of the magnetic-field-induced SHG intensity at 3.424 eV for different geometries at $B = 10$ T. Open circles represent measured data and lines show best fits following Eqs. (6)–(11). (a) $\mathbf{E}^{2\omega} \parallel \mathbf{E}^{\omega}$; fit according to Eq. (9). (b) $\mathbf{E}^{2\omega} \perp \mathbf{E}^{\omega}$; fit according to $I^{2\omega} \propto [a \sin\varphi + b \sin\varphi \cos^2\varphi]^2$, with $a/b = 1/2$; a and b represent the spin Zeeman contributions of s and p type, respectively, see Figs. 16(b) and 16(j). (c) $\mathbf{E}^{2\omega} \parallel \mathbf{B}$; fit according to Eq. (7). (d) $\mathbf{E}^{2\omega} \perp \mathbf{B}$; fit according to $I^{2\omega} \propto \cos^4\varphi$.

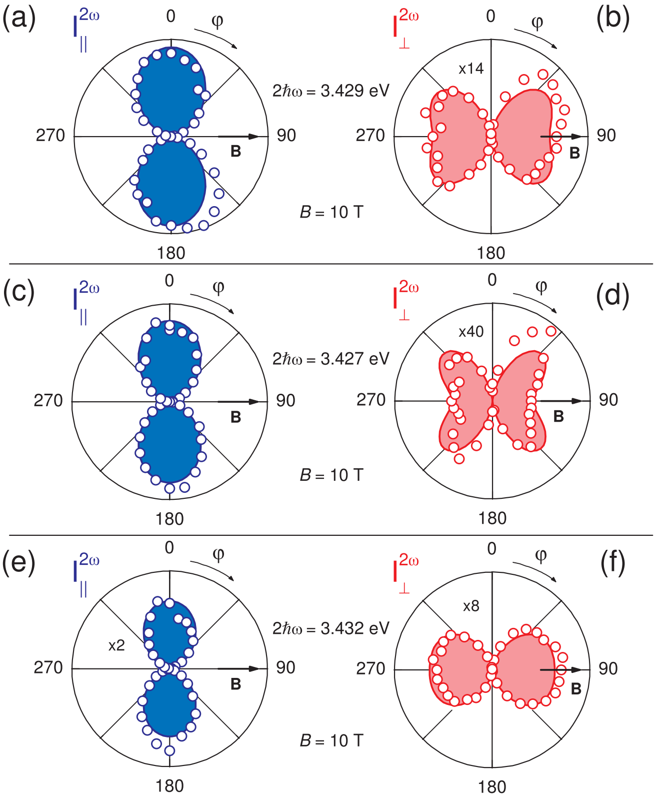

FIG. 11. (Color online) Angular dependences of the magnetic-field-induced SHG intensity for different energies at $B = 10$ T. Open blue circles give the measured intensity $I_\parallel^{2\omega}$ for $\mathbf{E}^{2\omega} \parallel \mathbf{E}^{\omega}$ and open red circles give the measured intensity $I_\perp^{2\omega}$ for $\mathbf{E}^{2\omega} \perp \mathbf{E}^{\omega}$. Solid lines show best fits according to $I_\parallel^{2\omega} \propto \chi_{yyy}^2 \cos^2(\varphi)$ [see Eq. (9)] and $I_\perp^{2\omega} \propto [a \sin\varphi + b \sin\varphi \cos^2\varphi]^2$; a and b represent the spin Zeeman contributions of s- and p-type excitons, respectively, see Figs. 16(b) and 16(j). The ratio $I_\parallel^{2\omega}/I_\perp^{2\omega}$ indicates the dominance of the magneto-Stark contribution compared to the spin Zeeman contribution. (a) and (b) $2\hbar\omega = 3.429$ eV; $I_\parallel^{2\omega}/I_\perp^{2\omega} \approx 14/1$; $I_\perp^{2\omega}$ with $a/b = 1/1$. (c) and (d) $2\hbar\omega = 3.427$ eV; $I_\parallel^{2\omega}/I_\perp^{2\omega} \approx 40/1$; $I_\perp^{2\omega}$ with $a/b = 3/4$. (e) and (f) $2\hbar\omega = 3.432$ eV; $I_\parallel^{2\omega}/I_\perp^{2\omega} \approx 4/1$; $I_\perp^{2\omega}$ with $a/b = 2/1$.

and crystallographic SHG have comparable values. On the other hand, the $1s_{\mathrm{L}}(C)$ state is not strongly modified by the magnetic-field-induced contributions, compare amplitudes in Figs. 12(c) and 12(d).

C. Temperature dependence

Figure 13 compares the crystallographic SHG intensities $I_\parallel^{2\omega}$ recorded at 1.6 and 128 K. While the off-resonant contribution has comparable intensity, the exciton SHG signals strongly decrease with rising temperature. A closer look at the detailed evolutions of the peak intensities shows that all $1s$ states and the X-line intensities decrease slower with temperature than the $2p_{x,y}(A)$ states, compare the results shown in Fig. 14(a). At the same time, the full width at half maximum (FWHM) of the $2p_{x,y}(A)$ line increases much faster than those of the $1s_{\mathrm{L}}(C)$ state and the X line, see Fig. 14(b). The magnetic field influences the temperature dependence only slightly: The magnetic-field-induced signals show a similar behavior as the crystallographic ones; the closed and open dots in Fig. 14(a) give the temperature dependences for zero field and $B = 7$ T, respectively. We conclude that these dependences are rather independent of the SHG generating mechanism. An explanation based on our theoretical model will be discussed in Sec. VI.

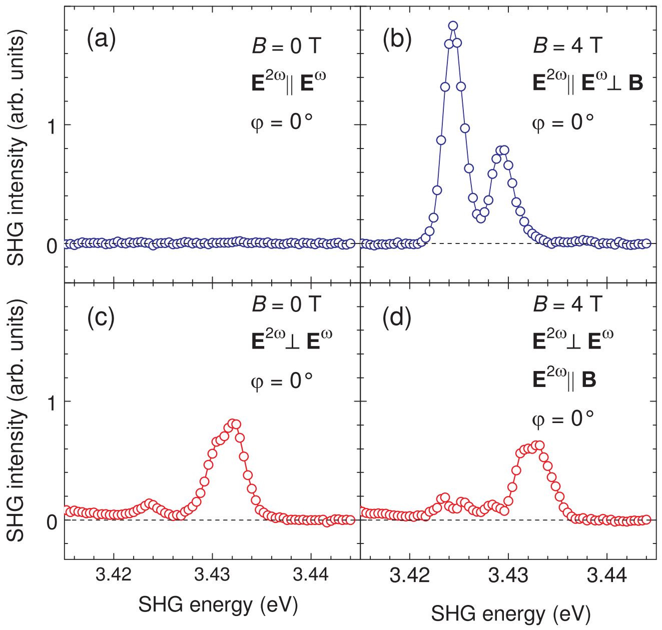

FIG. 12. (Color online) Crystallographic and magnetic-field-induced SHG in the spectral range of the $2s/2p(A,B)$ and $1s_{\mathrm{L}}(C)$ excitons measured for the tilted geometry with $\theta \approx 45^\circ$. $T = 1.6$ K. (a) There is no crystallographic contribution to $I_\parallel^{2\omega}$ for $\varphi(\mathbf{E}^{\omega}) = 0^\circ$. (b) Pure magnetic-field-induced SHG signals at $B = 4$ T for $I_\parallel^{2\omega}$ and $\varphi(\mathbf{E}^{\omega}) = 0^\circ$ contributed by the $2s/2p(A,B)$ excitons. (c) and (d) $I_\perp^{2\omega}$ for the $1s_{\mathrm{L}}(C)$ exciton does not change significantly from $B = 0$ to 4 T.

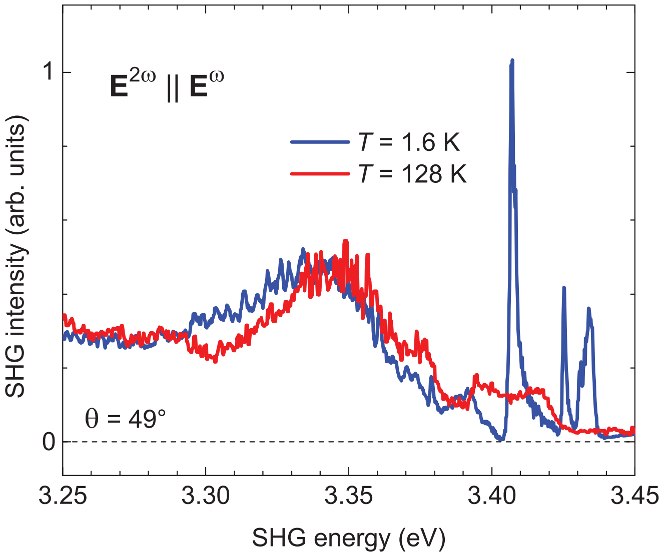

FIG. 13. (Color online) Crystallographic SHG spectra of ZnO for $\mathbf{E}^{2\omega} \parallel \mathbf{E}^{\omega}$ at $\varphi = 90^\circ$, measured at $T = 1.6$ K (blue line) and 128 K (red line).

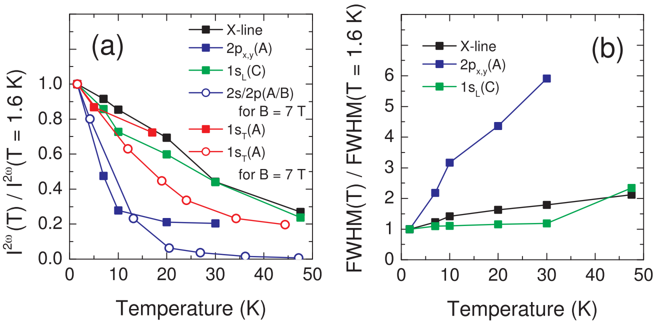

FIG. 14. (Color online) (a) Normalized SHG intensity vs temperature for different photon energies. Crystallographic signals of the $1s_L(C)$ exciton (green squares) and the unidentified X line (black squares) decrease to about 20% at $T = 50$ K. Crystallographic signal of the $2p_{x,y}(A)$ state (blue squares) and magnetic-field-induced signal of $2s/2p(A,B)$ states (open blue circles) show a fast decay and vanish in the background for $T > 30$ K. For $B = 7$ T the temperature dependences of the $1s$ and $2s/2p$ states change only slightly compared to the zero-field case, see open symbols. (b) Normalized FWHM extracted from SHG measurements at different energies. In contrast to the slow temperature increase for the $1s_L(C)$ exciton (green squares) and the X line (black squares) the FWHM of the $2p_{x,y}(A)$ exciton (blue squares) shows a rapid increase with temperature.

D. Joint action of magnetic and electric field

An applied electric field modifies the wave functions of the exciton states and, therefore, offers another promising option for SHG spectroscopy. The electric field is a polar vector of odd parity, in contrast to the even parity magnetic field, so that it can mix exciton wave functions of opposite parity.

The two spectra in Fig. 15(b) demonstrate the effect of an applied electric field on SHG spectra for the $2s/2p(A,B)$ excitons in ZnO at zero magnetic field. In the absence of electric field the residual SHG amplitude (about 1% of those previously discussed) originates from small strain caused by the sample holder with electrical contacts. Application of an electric field perpendicular to the z axis $\mathbf{E} \perp \mathbf{k} \parallel \mathbf{z}$ leads to an increase in the SHG signal.

The electric field effect is much more pronounced in combination with an applied magnetic field $\mathbf{E} \perp \mathbf{B}$, see Fig. 15(a). Here the SHG amplitude is initially gained by applying a magnetic field of +1 T and then tuned by adding an electric field of ±550 V/cm. The SHG signal increases for positive electric fields and decreases for negative fields. The rotational anisotropies of these signals are not changed by the electric field. The variation of the integral SHG intensity with electric field strength is shown in the inset of Fig. 15(a). Such a behavior that a weak effect (here induced by the electric field) is enhanced when combined with a stronger effect (by the magnetic field) is known in SHG spectroscopy when these effects interfere with each other, see, e.g., Eq. (3) in Ref. 35.

Resistivity measurements have shown that the incident laser beam reduces the sample resistivity enormously (by several orders of magnitude), when twice the fundamental photon energy $2\hbar\omega$ comes close to that of the $2p$ exciton states, see Fig. 15(c). The resistivity is not instantaneously restored when the laser is switched off.

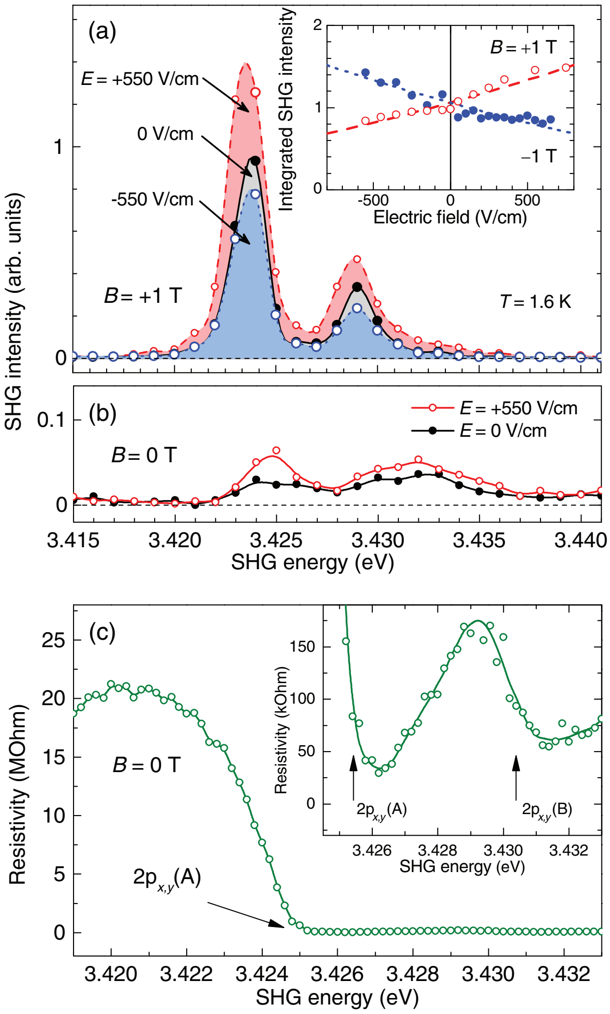

FIG. 15. (Color online) (a) SHG spectra in the range of the $2s/2p(A,B)$ excitons in ZnO subject to magnetic field and combined electric and magnetic fields. An applied electric field of $E = \pm 550$ V/cm corresponds inside the crystal to the field $E/\epsilon^{\perp}$, where $\epsilon^{\perp} = 7.40$ is the static dielectric permittivity perpendicular to the hexagonal z axis. Inset shows integrated intensity in the spectral range 3.417–3.438 eV as function of electric field for $B = +1$ and -1 T. Symbols are experimental data and lines give best fits according to $I^{2\omega} \propto (\pm B + \gamma E)^2$ with $\gamma = 2.5 \times 10^{-4}$. (b) SHG spectra without applied magnetic field. The red line demonstrates electric field effect [intensity is increased by a factor of 4 compared to (a)]. (c) Measured resistivity of the sample at $B = 0$ T showing a strong drop by about three orders of magnitude when $2\hbar\omega$ becomes close to the $2p_{y,x}(A,B)$ excitons. Inset shows a close-up (×100) of this region.

V. THEORY OF SHG AT EXCITON RESONANCES

A. General consideration

Theoretical studies of SHG were performed for many model semiconductors, see, e.g., Refs. 57–67. These publications analyze the generation of the second and higher harmonics by band theory or first-principle calculations, while exciton contributions have remained essentially unexplored. The complex experimentally observed exciton SHG signals for ZnO in external fields as reported here demands development of a corresponding microscopic theory.

In this section we focus on SHG effects in resonance with exciton states. This requires the analysis of the wave function symmetries for different exciton states and their modifications in external magnetic and electric fields. We present a theoretical analysis for the excitons in ZnO with wurtzite-type crystal structure. The developed theoretical approach, however, can be readily applied to other semiconductors. In particular, most of the suggested mechanisms of magnetic- and electric-field-induced SHG at the exciton resonances should exist also in other materials.

To analyze SHG in close vicinity of an exciton resonance we write the nonlinear optical susceptibilities $\chi_{ijl}(\mathcal{E}_{\rm exc},\mathbf{k}_{\rm exc},\mathbf{B},\mathbf{E})$ introduced in Eq. (3) for each exciton energy $\mathcal{E}_{\rm exc} = 2\hbar\omega$ in general form as

$$\begin{aligned}\chi_{ijl}(\mathcal{E}_{\rm exc},\mathbf{k}_{\rm exc},\mathbf{B},\mathbf{E}) \\ \propto \sum_{v} \frac{\langle G|\hat{V}_i^{2\omega}|\Psi_{\rm exc}\rangle\langle\Psi_{\rm exc}|\hat{V}_j^{\omega}|\psi_v\rangle\langle\psi_v|\hat{V}_l^{\omega}|G\rangle}{(\mathcal{E}_{\rm exc}-2\hbar\omega-i\Gamma_{\rm exc})(\mathcal{E}_v-\hbar\omega)} \\ \approx \frac{i}{\Gamma_{\rm exc}}\langle G|\hat{V}_i^{2\omega}|\Psi_{\rm exc}\rangle M^{\rm 2ph}_{{\rm exc},G}.\end{aligned} \tag{4}$$

Here $|G\rangle$ denotes the unperturbed ground state with zero energy, $|\psi_v\rangle$ describes intermediate virtual states with energy $\mathcal{E}_v$, $|\Psi_{\rm exc}\rangle$ describes the exciton state, and $\Gamma_{\rm exc}$ is the exciton damping constant. The summation in Eq. (4) is carried out over all intermediate states satisfying the symmetry selection rules for the two-photon transition from the ground to the exciton state described by the matrix element $M^{\rm 2ph}_{{\rm exc},G}$.

To account for the effects of the external electric and magnetic fields we consider the geometry where the crystallographic SHG signals are suppressed, namely $\mathbf{k}_{\rm exc} \parallel \mathbf{k} \parallel \mathbf{z}$, $\mathbf{B} \parallel \mathbf{x}$, and $\mathbf{E} \parallel \mathbf{y}$. In this case the incoming photon field is described by $\mathbf{E}^{\omega} = (E^{\omega}_x,E^{\omega}_y,0)$ so that the outgoing polarization can be written as $\mathbf{P}^{2\omega}_{\rm eff} = (P^{2\omega}_{{\rm eff},x},P^{2\omega}_{{\rm eff},y},0)$.

The perturbation caused by the photon field $\mathbf{E}^{\omega}(\mathbf{r},t)$ is described by $(ie/m_0\omega)[\mathbf{E}^{\omega}(\mathbf{r},t)\hat{\mathbf{p}}]$, where e and m_0 are the charge and mass of free electron and $\hat{\mathbf{p}}$ is the momentum operator. Then the perturbation $\hat{V}^{\omega}_{x(y)}$ is given by

$$\begin{aligned}\hat{V}^{\omega}_{x(y)} &= \frac{ie}{m_0\omega}\hat{p}_{x(y)}\exp(ik_z r_z) \\ &\approx \frac{ie}{m_0\omega}\hat{p}_{x(y)}(1+ik_z r_z+\cdots),\end{aligned} \tag{5}$$

where $\hat{p}_{x(y)}$ are the projections of the momentum operator $\hat{\mathbf{p}}$ on the light polarization components x or y, respectively. For $\hat{V}^{2\omega}_{x(y)}$ one should substitute k_z by $2k_z$ in Eq. (5) and everywhere below, as well as ω by 2ω. We are interested in the lowest order effects in k_z, that is zero-order independent of k_z, if it exists, or first-order linear in k_z. Therefore, we keep only two terms in the expansion of $\exp(ik_z r_z) = 1 + ik_z r_z$ and consider the perturbation in the form $\hat{V}^{\omega}_{x(y)} = \hat{D}^{\omega}_{x(y)} + \hat{Q}^{\omega}_{x(y)z}$. The first term $\hat{D}^{\omega}_{x(y)} = (ie/m_0\omega)\hat{p}_{x(y)}$ corresponds to the electric-dipole (ED) approximation for which the matrix elements can be replaced[68] by the matrix elements of the dipole operator $er_{x(y)}/\hbar$. The operator $\hat{Q}^{\omega}_{x(y)z} = -(ek_z/m_0\omega)\hat{p}_{x(y)}r_z$ includes the electric-quadrupole (EQ) and the magnetic-dipole (MD) contributions where the matrix elements can be replaced[68] by the sum of matrix elements of the electric-quadrupole operator $\hat{Q}^{\omega,q}_{x(y)z} = -(iek_z/2)r_{x(y)}r_z$ and the magnetic-dipole operator $\hat{Q}^{\omega,m}_{x(y)z} = \pm(e\hbar k_z/2m_0\omega)\hat{L}_{y(x)}$. Here $\hat{\mathbf{L}}$ is the orbital momentum operator. Depending on the perturbation $\hat{V}^{\omega}$ and $\hat{V}^{2\omega}$ involved in the two-photon absorption and one-photon emission, respectively, we denote the resulting three-photon SHG process as $X^{2w}Y^{\omega}Z^{\omega}$, where the X,Y,Z are either D (ED) or Q (EQ + MD). We emphasize, that the presence of EQ or MD transition for one of the steps either excitation or emission, leads to a linear dependence of the susceptibility on k_z.

In ZnO, the direct ED transitions between the valence and conduction band states are allowed. The strongest one-photon process for $\mathbf{k} \parallel \mathbf{z}$ are the excitation of the $(s \times \Gamma_5)$ states or the emission from them. The respective matrix elements can be written as $D^{\omega,a}$ or $D^{2\omega,a}$, where the index a denotes "allowed" transition within the ED approximation according to the notation of Elliot.[69] In contrast, the one-photon ED "forbidden" transitions to the $2p$ excitons in noncentrosymmetric wurtzite semiconductors like ZnO may occur because the valence and conduction band states do not have pure even or odd parities. These transitions are much weaker compared to the s exciton transitions and can be described by the matrix elements $D^{\omega,f}$ or $D^{2\omega,f}$, where the index f denotes the forbidden character within the ED approximation.[69] In the used geometry such forbidden transitions are possible only for the $2p_{x,y}$ states, and not for the $2p_z$ state. Alternatively, the one-photon emission from all three $2p_x$, $2p_y$, and $2p_z$ states may occur due to magnetic-dipole transitions described by the matrix element $Q^{2\omega,m}$.

The strongest two-photon process in ZnO is the excitation of the $2p$ exciton states. It is ED allowed, exploiting intermediate virtual states in the valence or conduction band. Such a process involves a transition between valence and conduction band states and another transition between s and p envelopes in the same energy band. The relevant two-photon matrix element is $M^{\rm 2ph}_{2p,G} \propto D^{\omega,a}D^{\omega,f}$. On the other hand, the direct two-photon absorption by the s exciton states in noncentrosymmetric semiconductors may occur within the ED approximation via the intermediate virtual states in remote bands.[70] In this case the two-photon matrix element is $M^{\rm 2ph}_{s,G} \propto D^{\omega,a}D^{\omega,a}$. However, such processes are much weaker than those for the $2p$ excitons.[71] Alternatively, the s states can be excited in the two-photon process when the first transition is a MD transition (or ED transition of forbidden character) to the $2p_{x,y}$ states and the second one is an ED transition of forbidden character between the s and the p envelopes. In this case the two-photon matrix element is $M^{\rm 2ph}_{s,G} \propto D^{\omega,f}Q^{\omega,m}$ (or $M^{\rm 2ph}_{s,G} \propto D^{\omega,f}D^{\omega,f}$).

Important information on the symmetry of the exciton states involved in the SHG process is provided by the SHG rotational anisotropies. According to Eq. (3) the SHG intensity is given by

$$I^{2\omega}_{\perp\mathbf{B}} \propto |\chi_{yyy}\cos^2\varphi + \chi_{yxx}\sin^2\varphi|^2, \tag{6}$$

if $\mathbf{E}^{2\omega}\perp\mathbf{B}$; and by

$$I^{2\omega}_{\parallel\mathbf{B}} \propto |\chi_{xxy}\sin(2\varphi)|^2, \tag{7}$$

for the $\mathbf{E}^{2\omega}\parallel\mathbf{B}$ geometry. Here φ is the angle between $\mathbf{E}^{\omega}$ and the y axis. Note that $\mathbf{B}\perp\mathbf{y}$. For parallel polarization $\mathbf{E}^{2\omega}\parallel\mathbf{E}^{\omega}$

TABLE I. Different mechanisms providing SHG in external electric and magnetic fields at the $1s(A,B,C)$, $2s(A,B,C)$, and $2p(A,B)$ exciton resonances in ZnO. Experimental geometry: $\mathbf{k} \parallel \mathbf{z}$, $\mathbf{E} = (0,E_y,0)$, and $\mathbf{B} = (B_x,0,0)$. Due to symmetry $\chi_{xxy} = \chi_{xyx}$. The symbols indicate the different mechanisms: ♦ for the spin Zeeman effect, ♠ for the Stark, the magneto-Stark, and the orbital Zeeman effect, ★ for the spin Zeeman effect for $2p_y$, and ♣ for the spin Zeeman effect for $2p_x$. The corresponding rotational anisotropies are given in Fig. 16.

Mechanisms	$1s$, $2s$	$2s/2p_y$	$2p_z/2p_y$	$2p_y$	$2p_x$
Stark effect $D_i^{2\omega}D_j^{\omega}D_l^{\omega}$ $E_y \neq 0$, $B_x = 0$		$\chi_{yyy} = 2\chi_{xxy} \neq 0$, $\chi_{yxx} = 0$ ♠			
Magneto-Stark effect $D_i^{2\omega}D_j^{\omega}D_l^{\omega}$ $E_y = 0$, $B_x \neq 0$		$\chi_{yyy} = 2\chi_{xxy} \neq 0$, $\chi_{yxx} = 0$ ♠			
Spin Zeeman effect $D_i^{2\omega}D_j^{\omega}Q_l^{\omega,m}$ $E_y = 0$, $B_x \neq 0$	$\chi_{yyy} = \chi_{yxx} \neq 0$, $\chi_{xxy} = 0$ ♦				
Spin Zeeman effect $Q_i^{2\omega,m}D_j^{\omega}D_l^{\omega}$ $E_y = 0$, $B_x \neq 0$				$\chi_{yyy} \neq 0$, ★ $\chi_{xxy} = \chi_{yxx} = 0$	$\chi_{xxy} \neq 0$, ♣ $\chi_{yyy} = \chi_{yxx} = 0$
Orbital Zeeman effect $Q_i^{2\omega,m}D_j^{\omega}D_l^{\omega}$ $E_y = 0$, $B_x \neq 0$			$\chi_{yyy} = 2\chi_{xxy} \neq 0$, $\chi_{yxx} = 0$ ♠		

one obtains

$$I_{\parallel}^{2\omega} \propto \cos^2\varphi|\chi_{yyy}\cos^2\varphi + (\chi_{yxx} + 2\chi_{xxy})\sin^2\varphi|^2. \tag{8}$$

In a hexagonal $6mm$ crystal the relation $\chi_{yyy} = \chi_{yxx} + 2\chi_{xxy}$ is fulfilled[43] so that

$$I_{\parallel}^{2\omega} \propto |\chi_{yyy}\cos\varphi|^2. \tag{9}$$

For perpendicular polarization $\mathbf{E}^{2\omega} \perp \mathbf{E}^{\omega}$ one finds

$$I_{\perp}^{2\omega} \propto \sin^2\varphi|(\chi_{yyy} - 2\chi_{xxy})\cos^2\varphi + \chi_{yxx}\sin^2\varphi|^2, \tag{10}$$

and if the relation $\chi_{yyy} = \chi_{yxx} + 2\chi_{xxy}$ is fulfilled, then

$$I_{\perp}^{2\omega} \propto |\chi_{yxx}\sin\varphi|^2. \tag{11}$$

Below we will show that a magnetic field applied perpendicular to the hexagonal z axis may reduce the symmetry of an exciton state and, consequently, it violates the relation $\chi_{yyy} = \chi_{yxx} + 2\chi_{xxy}$.

In the following subsections we will proceed with the analysis of different specific mechanisms of the field-induced mixing of exciton states and derive the corresponding nonlinear optical susceptibilities. The results of this analysis are summarized in Table I. Relations between χ_{yyy}, χ_{yxx}, and χ_{xxy} allow one to model the rotational anisotropies for each particular mechanism. We note that the admixture of exciton states in applied fields may lead to the dependence of the wave function Ψ_{exc} and the respective energy $\mathcal{E}_{\text{exc}}$ on the exciton wave vector $\mathbf{k}_{\text{exc}}$, as well as on B_x and E_y. These complex perturbations may lead to a nonlinear dependence of the susceptibilities $\chi_{ijl}(\mathcal{E}_{\text{exc}},k_{\text{exc}},B_x,E_y)$ on B_x, E_y, and k_z, via $k_{\text{exc}} = 2nk_z$. They act in addition to those arising from the second term in the expansion of $\exp(ik_z z)$ according to Eq. (5).

B. SHG and exciton Stark effect (E ⊥ k∥z)

Let us first consider the SHG signals induced by an external electric field E_y which mixes the $2s$ and $2p_y$ exciton states of opposite parity due to the Stark effect for the A and B excitons. However, it does not affect their spin states. Two polariton branches can be formed for each of the mixed $2s/2p$ exciton states. The new energies $\mathcal{E}_{\text{exc}} = \mathcal{E}^{\pm}_{2s_{\text{T}}/2p_y}$ for the transversal LPB and $\mathcal{E}_{\text{exc}} = \mathcal{E}^{\pm}_{2s_{\text{L}}/2p_y}$ for the transversal UPB are given in the Appendix. The resulting wave functions of the mixed states in Eq. (A3) are constructed from the $2s$ and $2p_y$ components. In this process, all matrix elements for excitation and emission in Eq. (4) become allowed in the ED approximation $\hat{V}^{\omega(2\omega)}_{x(y)} = \hat{D}^{\omega(2\omega)}_{x(y)}$. We denote the corresponding SHG as $D^{2\omega}D^{\omega}D^{\omega}$ as shown in the first row of Table I. The corresponding SHG signals can be observed only when the incoming light has a nonzero component $E^{\omega}_y \neq 0$ responsible for excitation of the $2p_y$ state. Therefore, for this process $\chi_{yxx} = 0$ and the resulting electric-field-induced susceptibilities $\chi_{yyy} = 2\chi_{xxy} = 2\chi_{xyx}$ are proportional to the product of the wave function admixture coefficients in Eqs. (A4) and (A5). They can be written as

$$\chi_{yyy}(\mathcal{E}^{\pm}_{2s/2p_y},k_{\text{exc}},0,E_y) \propto C_{2s}(E_y)C_{2p_y}(E_y) = -\frac{3eE_y a_{\text{B}}\left(\mathcal{E}_{2p_y} - \mathcal{E}^{\pm}_{2s/2p_y}\right)}{(3eE_y a_{\text{B}})^2 + \left(\mathcal{E}_{2p_y} - \mathcal{E}^{\pm}_{2s/2p_y}\right)^2}, \tag{12}$$

where a_{B} is the exciton Bohr radius. One sees that these electric-field-induced susceptibilities do not depend on the absolute value of k_z, however, the direction of $\mathbf{k}$ parallel to the z axis is important. If the electric field perturbation energy is much smaller than the zero-field splitting of the exciton states, $|eE_y a_{\text{B}}| \ll |\mathcal{E}_{2p} - \mathcal{E}_{2s_{\text{T(L)}}}|$, then the susceptibilities depend linearly on E_y. However, for larger fields a saturation is expected because for $|eE_y a_{\text{B}}| \gg |\mathcal{E}_{2p} - \mathcal{E}_{2s_{\text{T(L)}}}|$ the susceptibilities become independent of E_y.

C. SHG and magnetic-field effects on excitons ($\mathbf{B} \perp \mathbf{k} \| \mathbf{z}$)

The effect of an applied magnetic-field $\mathbf{B}$ on excitons shows more facets than an electric field. We will discuss several mechanisms acting when the magnetic field is applied along the x axis, $\mathbf{B} = (B_x,0,0)$.

(1) *The spin Zeeman effect*, which mixes the exciton spin states through a perturbation $\propto (\sigma_x B_x)$, where σ_x is the corresponding Pauli matrix.

(2) *The orbital Zeeman effect*, which affects the p states having nonzero envelope orbital momentum $L = 1$ and mixes the $2p_z$ and $2p_y$ states by a perturbation $\propto (L_x B_x)$.

(3) *The magneto-Stark effect*.[72–76] This effect arises from the oppositely directed Lorentz forces acting on electron and hole in a magnetic field during the exciton center-of-mass motion. The resulting perturbation of the exciton wave function is equivalent to the effect of an effective electric field $\mathbf{E}_{\text{eff}}$ acting on the exciton at rest:

$$\mathbf{E}_{\text{eff}} = \frac{\hbar}{M_{\text{exc}}} [\mathbf{k}_{\text{exc}} \times \mathbf{B}]. \tag{13}$$

Here $M_{\text{exc}} = m_e + m_h$ denotes the exciton effective mass. In the given geometry the effective electron and hole masses for motion parallel to the hexagonal z axis $\mathbf{k}_{\text{exc}} \parallel \mathbf{z}$ and $\mathbf{E}_{\text{eff}} \parallel \mathbf{y}$ have to be used: $m_e = m_e^{\|}$ and $m_h = m_h^{\|}$.

The diamagnetic shift of the exciton energy occurs for all states and is state dependent.[45,46] It does not directly lead to a state mixing, but can enhance mixing by other mechanisms due to favorable energy shifts, bringing states closer to each other.

It is important that the external magnetic-field B_x can mix exciton states of different symmetry allowing two-photon resonant excitation and one-photon resonant emission at a given energy and thus leading to SHG signals. The Zeeman spin mixing may induce SHG signals for one particular envelope exciton state. The orbital Zeeman effect and the magneto-Stark effect mix states with different envelope functions. The strength of this mixing depends on the energy separation of these states at zero field. At a given exciton energy the SHG signal might be induced by several mixing mechanisms acting simultaneously. Below we analyze these mechanisms in detail for each particular exciton state.

1. Magnetic-field-induced SHG for s-type excitons due to spin Zeeman effect

The spin states of the s-type excitons depend on the symmetries of the conduction and valence bands. For excitons formed from the conduction band of Γ_7 symmetry and the valence band of Γ_7 symmetry the resulting exciton states are of Γ_5, Γ_1, and Γ_2 symmetry, split from each other by the electron-hole exchange interaction. Examples of such states are the A and C excitons in ZnO, or the B and C excitons in GaN. The dipole-allowed Γ_5 state can occur for a one-photon process and forms two polariton branches in the given geometry. The Γ_1 state can become excited by a two-photon process if one of the involved photons is due to the quadrupole perturbation or due to the involvement of intermediate virtual states in remote bands.[70] As a result, the $1s$ exciton states of the A and C excitons might be observed in the SHG spectrum due to the Zeeman spin mixing of the Γ_{5y} and Γ_1 states. The energies of the new mixed polariton states $\mathcal{E}_{\Gamma_{5y}/\Gamma_1}$ are given by Eq. (A8) in the Appendix. The resulting wave functions of the mixed states described by Eq. (A9) are constituted by both Γ_{5y} and Γ_1 components.

The two-photon excitation of the s state might occur through an electric-dipole/electric-dipole ($D^{\omega,a} D^{\omega,a}$) or an electric-dipole/magnetic-dipole ($D^{\omega} Q^{\omega,m}$) process as discussed above. For the sake of clarity we consider the second case in detail. It is represented by the process $D^{2\omega} D^{\omega} Q^{\omega,m}$ in the third row of Table I. Then the SHG process involves a matrix element for the two-photon excitation with $\hat{V}^{\omega}_{x(y)} = \hat{Q}^{\omega,m}_{x(y)z}$ for one of the photons and $\hat{V}^{\omega}_{x(y)} = \hat{D}^{\omega}_{x(y)}$ for the second photon. The subsequent one-photon ED emission with $\hat{V}^{2\omega}_{y} = \hat{D}^{2\omega}_{y}$ is allowed through the $s_{\Gamma_{5y}}$ part of the exciton wave function, so that $\chi_{xxy} = 0$. The resulting magnetic-field-induced nonzero susceptibilities $\chi_{yyy} = \chi_{yxx}$ are given by

$$\begin{aligned} &\chi_{yyy}\big(\mathcal{E}^{\pm}_{\Gamma_{5y}/\Gamma_1}, k_{\text{exc}}, B_x, 0\big) \\ &\quad \propto C_{\Gamma_5}(B_x) C_{\Gamma_1}(B_x)(k_z a_0) \\ &\quad = -\frac{2\mu_{\text{B}} g_{\text{exc}} B_x \big(\mathcal{E}_{\Gamma_5} - \mathcal{E}^{\pm}_{\Gamma_{5y}/\Gamma_1}\big)(k_z a_0)}{(\mu_{\text{B}} g_{\text{exc}} B_x)^2 + 4\big(\mathcal{E}_{\Gamma_5} - \mathcal{E}^{\pm}_{\Gamma_{5y}/\Gamma_1}\big)^2}. \end{aligned} \tag{14}$$

Here g_{exc} is the exciton g factor, a_0 is the lattice constant, and $\mathcal{E}^{\pm}_{\Gamma_5}$ is the zero-field energy of the LPB or UPB exciton-polariton, respectively. The linear dependence on k_z enters through the matrix element of the magnetic-dipole excitation with $\hat{V}^{\omega}_{x(y)} = \hat{Q}^{\omega,m}_{x(y)z}$. If the exciton Zeeman splitting $|\mu_{\text{B}} g_{\text{exc}} B_x|$ is much smaller than the zero-field splitting of the corresponding exciton state, then the susceptibilities depend linearly on B_x so that the SHG intensity follows a B^2 dependence.

For s-symmetry states, for which the SHG process is allowed by the Zeeman spin effect, calculations show that $\chi_{yyy} = \chi_{yxx} \neq 0$ and $\chi_{xxy} = \chi_{xyx} = 0$. The intensity of the SHG signal polarized perpendicular to the magnetic field $I^{2\omega}_y \propto |\chi_{yyy}(\mathcal{E}_{\Gamma_{5y}/\Gamma_1}, k^{\omega}_z, B_x, 0)|^2$ does not depend on the excitation polarization direction, while the signal polarized parallel to the magnetic field vanishes: $I^{2\omega}_x \propto |\chi_{xxy}(\mathcal{E}_{\Gamma_{5y}/\Gamma_1}, k_z, B_x, 0)|^2 = 0$. For the parallel $\mathbf{P}^{2\omega}_{\text{eff}} \parallel \mathbf{E}^{\omega}$ and the crossed $\mathbf{P}^{2\omega}_{\text{eff}} \perp \mathbf{E}^{\omega}$ geometries SHG signals of the same amplitude are predicted. Their anisotropies are described by $I^{2\omega}_{\|} \propto |\chi_{yyy}|^2 \cos^2\varphi$ and $I^{2\omega}_{\perp} \propto |\chi_{yxx}|^2 \sin^2\varphi$.

For excitons formed by the conduction band of Γ_7 symmetry and the valence band of Γ_9 symmetry the resulting exciton states are of Γ_5 and Γ_6 symmetry. Examples are the B excitons in ZnO and the A excitons in GaN. The Zeeman effect mixes the dipole-allowed Γ_5 states and the dark Γ_6 state. In addition, one has to take into account the exchange interaction between the Γ_5 components of the A and B excitons which may lead to SHG from the Γ_{5y}/Γ_6 exciton states with the same properties as described above for the Γ_{5y}/Γ_1 excitons. In addition, the Γ_{5y}/Γ_6 exciton states can be excited via the $D^{\omega,a} D^{\omega,a}$ process.

2. Magnetic-field-induced SHG for mixed $2s/2p$ excitons

Let us now consider the effect of the effective electric field $E_{\text{eff}} = \frac{\hbar}{M_{\text{exc}}} k_{\text{exc}} B_x$ on the exciton states. The mixing of $2s$ and $2p_y$ states of opposite parity induced thereby is similar to that caused by the Stark effect due to an external electric field. Simultaneously, another type of mixing occurs due to the Zeeman orbital effect, but this mechanism mixes the $2p_z$ and $2p_y$ states of the same parity. The resulting energies $\mathcal{E}^i_{2s/2p_z/2p_y}$ ($i = 1,2,3$) of the mixed $2s/2p_z/2p_y$ polariton branches are listed in Eq. (A16). The appropriate wave functions in Eq. (A17) are constructed from all three contributing states with coefficients $C^i_{2s(2p_z,2p_y)}(B_x)$ given by Eqs. (A18)–(A20). As a result, all mixed states can be excited by two photons with polarization having a nonzero field component $E^\omega_y \neq 0$, which excites the Ψ_{2p_y} component. ED perturbations $\hat{V}^\omega_{x(y)} = \hat{D}^\omega_{x(y)}$ are associated with the first photon and the $\hat{V}^\omega_y = \hat{D}^\omega_y$ perturbation with the second photon. There are three possible mechanisms allowing observation of these mixed $2s/2p_z/2p_y$ states in one-photon emission: (i) emission due to the Ψ_{2s} component through the ED perturbation $\hat{V}^{2\omega}_{x(y)} = \hat{D}^{2\omega}_{x(y)}$; (ii) emission due to the Ψ_{2p_z} component through the magnetic-dipole perturbation $\hat{V}^{2\omega}_{x(y)} = \hat{Q}^{2\omega,m}_{x(y)z}$; and (iii) emission due to the Ψ_{2p_y} component through the magnetic-dipole perturbation $\hat{V}^{2\omega}_{x(y)} = \hat{Q}^{2\omega,m}_{x(y)z}$ or through the electric-dipole-forbidden process $\hat{V}^{2\omega}_y = \hat{D}^{2\omega,f}_{yz}$.

a. Magneto-Stark effect. In the first case (i) the mechanism responsible for the SHG signal is coupling of the $2s$ and $2p_y$ states via the magneto-Stark effect and ED emission of the $2s$ state. The $D^{2\omega}D^\omega D^\omega$ process in the second row of Table I corresponds to this mechanism. The resulting magnetic-field-induced nonzero susceptibilities $\chi_{yyy} = 2\chi_{xxy} = 2\chi_{xyx}$ are proportional to the product of admixed components in the corresponding wave functions:

$$\chi^{2s/2p_y}_{yyy}\left(\mathcal{E}^i_{2s/2p_z/2p_y}, k_{\text{exc}}, B_x, 0\right) \propto C^i_{2s}(B_x) C^i_{2p_y}(B_x). \quad (15)$$

The susceptibilities depend both on the magnetic field and the wave vector value only via the dependence on the effective electric field $E_{\text{eff}} = \gamma k_{\text{exc}} B_x$. This dependence is linear when the energy of the effective electric field is smaller than the zero-field splitting of the states and it saturates in the opposite limit.

b. Orbital Zeeman effect. In the second case (ii) the mechanism responsible for the SHG signal is due to coupling of the $2p_z$ and $2p_y$ states via the orbital Zeeman effect and magnetic-dipole emission from the $2p_z$ state. This is the $Q^{2\omega,m}D^\omega D^\omega$ process shown in the fifth row of Table I. This effect is expected to be much weaker than the magneto-Stark effect and not important at the energy where the $2s$ exciton is dominant. The resulting magnetic-field-induced nonzero susceptibilities $\chi_{yyy} = 2\chi_{xxy} = 2\chi_{xyx}$ can be written as

$$\chi^{2p_y/2p_z}_{yyy}\left(\mathcal{E}^i_{2s/2p_z/2p_y}, k_{\text{exc}}, B_x, 0\right) \propto k_z a_0 C^i_{2p_z}(B_x) C^i_{2p_y}(B_x). \quad (16)$$

The linear dependence on k_z comes from the matrix element of the magnetic-dipole perturbation $\hat{V}^{2\omega}_{x(y)} = \hat{Q}^{2\omega,m}_{x(y)z}$. Linear dependence of the χ on B_x is expected only for weak magnetic fields.

The rotational anisotropy patterns of the SHG intensities for the processes induced by the magneto-Stark and the orbital Zeeman effect are similar. The main feature for both of them is disappearance of the signal in crossed geometry $\mathbf{P}^{2\omega}_{\text{eff}} \perp \mathbf{E}^\omega$ because $I^{2\omega}_\perp(\mathcal{E}^i_{2s/2p_z/2p_y}) \propto |\chi_{yxx}|^2 = 0$ for any polarization direction of the excitation light $\mathbf{E}^\omega$. The SHG signal in the parallel geometry $\mathbf{P}^{2\omega}_{\text{eff}} \parallel \mathbf{E}^\omega$ can be modeled as $I^{2\omega}_\parallel \propto |\chi_{yyy}|^2 \cos^2\varphi$, while the signal polarized along the magnetic-field direction varies as $I^{2\omega}_x \propto |\chi_{xxy}|^2 \sin^2(2\varphi)$. Since $\chi_{yxx} = 0$, the signal polarized perpendicular to the magnetic-field direction can be described by $I^{2\omega}_y \propto |\chi_{yyy}|^2 \cos^4\varphi$.

3. SHG due to spin Zeeman effect on p states

a. The p_y state. For the $2p_y$ state the spin Zeeman effect provides only one nonzero susceptibility due to the process $Q^{2\omega,m}D^\omega D^\omega$ shown in the fourth row of Table I. This susceptibility can be written as

$$\chi^{2p_y}_{yyy}\left(\mathcal{E}^i_{2s/2p_z/2p_y}, k_{\text{exc}}, B_x, 0\right) \propto \tfrac{1}{2} k_z a_0 C^i_{2p_y}(B_x), \quad (17)$$

where the linear dependence on k_z comes from the matrix element of the magnetic-dipole perturbation $\hat{V}^{2\omega}_{x(y)} = \hat{Q}^{2\omega,m}_{x(y)z}$. We have neglected here the electron-hole spin exchange splitting of the p states. Note, that the magnetic-field-induced mixing of the $2s/2p_z/2p_y$ envelopes reduces $C_{2p_y(B_x)}$ for the states in vicinity to the $2p_y$ state and thus reduces the Zeeman contribution to the SHG signal.

The corresponding rotational anisotropy patterns for the $2p_y$ states are $I^{2\omega}_\parallel \propto |\chi_{yyy}|^2 \cos^6\varphi$, $I^{2\omega}_\perp \propto |\chi_{yyy}|^2 \cos^4\varphi \sin^2\varphi$, $I^{2\omega}_{\parallel\mathbf{B}} = 0$, and $I^{2\omega}_{\perp\mathbf{B}} \propto |\chi_{yyy}|^2 \cos^4\varphi$. Note that the relation $\chi_{yyy} = \chi_{yxx} + 2\chi_{xxy}$ valid for $6mm$ crystals[43] is broken because of the symmetry reduction by the magnetic-field B_x. This field, directed perpendicular to the z axis, lifts the degeneracy of the $2p_x$ and $2p_y$ states.

b. The p_x state. A similar spin Zeeman mechanism is acting on the $2p_x(A)$ exciton state, which is not mixed by the magnetic field with other p or s states. The p_x state can be excited by two photons with a polarization with nonzero field component $E^\omega_x \neq 0$ via the dipole perturbations $\hat{V}^\omega_{x(y)} = \hat{D}^\omega_{x(y)}$ for the first photon and $\hat{V}^\omega_x = \hat{D}^\omega_x$ for the second photon or vice versa. Emission is due to the Zeeman mixing of the Γ_5 and Γ_1 spin states and the magnetic-dipole perturbation $\hat{V}^{2\omega}_{x(y)} = \hat{Q}^{2\omega,m}_{x(y)z}$; the relevant process $Q^{2\omega,m}D^\omega D^\omega$ is shown in the fourth row of Table I. In fact it corresponds to the very same Zeeman mixing of spin states as for the $1s$ states. Differences occur in the two-photon absorption and the one-photon emission for the s and p states. The nonzero susceptibility $\chi_{xxy} = \chi_{xyx}$ relevant to these processes can be written as

$$\chi_{xxy}\left(\mathcal{E}_{2p_x}\right) \propto \tfrac{1}{2} k_z a_0, \quad (18)$$

where the linear dependence on k_z comes from the matrix element of the magnetic-dipole perturbation $\hat{V}^{2\omega}_{x(y)} = \hat{Q}^{2\omega,m}_{x(y)z}$.

There is no explicit dependence on the magnetic field in Eq. (18). However, a finite B_x is required for mixing the Γ_5 and Γ_1 spin states because without magnetic field the effect vanishes. B_x does not appear in Eq. (18) because we have neglected the exchange splitting of the mixed states, so that they have the same energy. However, even a very weak but finite magnetic field can mix them in equal strength. One may compare this case with Eq. (14), where there is a mixing of the Γ_5 and Γ_1 states that are split at $B = 0$. The magnetic-field dependence in Eq. (17) comes only from the B dependence of the contribution of the $2p_y$ component, given by $C_{2p_y}(B_x)$.

The SHG rotational anisotropy patterns for the $2p_x$ states via the spin Zeeman mixing are $I^{2\omega}_\parallel \propto |\chi_{xxy}|^2 \sin^2(2\varphi)\sin^2\varphi$, $I^{2\omega}_\perp \propto |\chi_{xxy}|^2 \sin^2(2\varphi)\cos^2\varphi$, $I^{2\omega}_{\parallel\mathbf{B}} = |\chi_{xxy}|^2 \sin^2(2\varphi)$, and

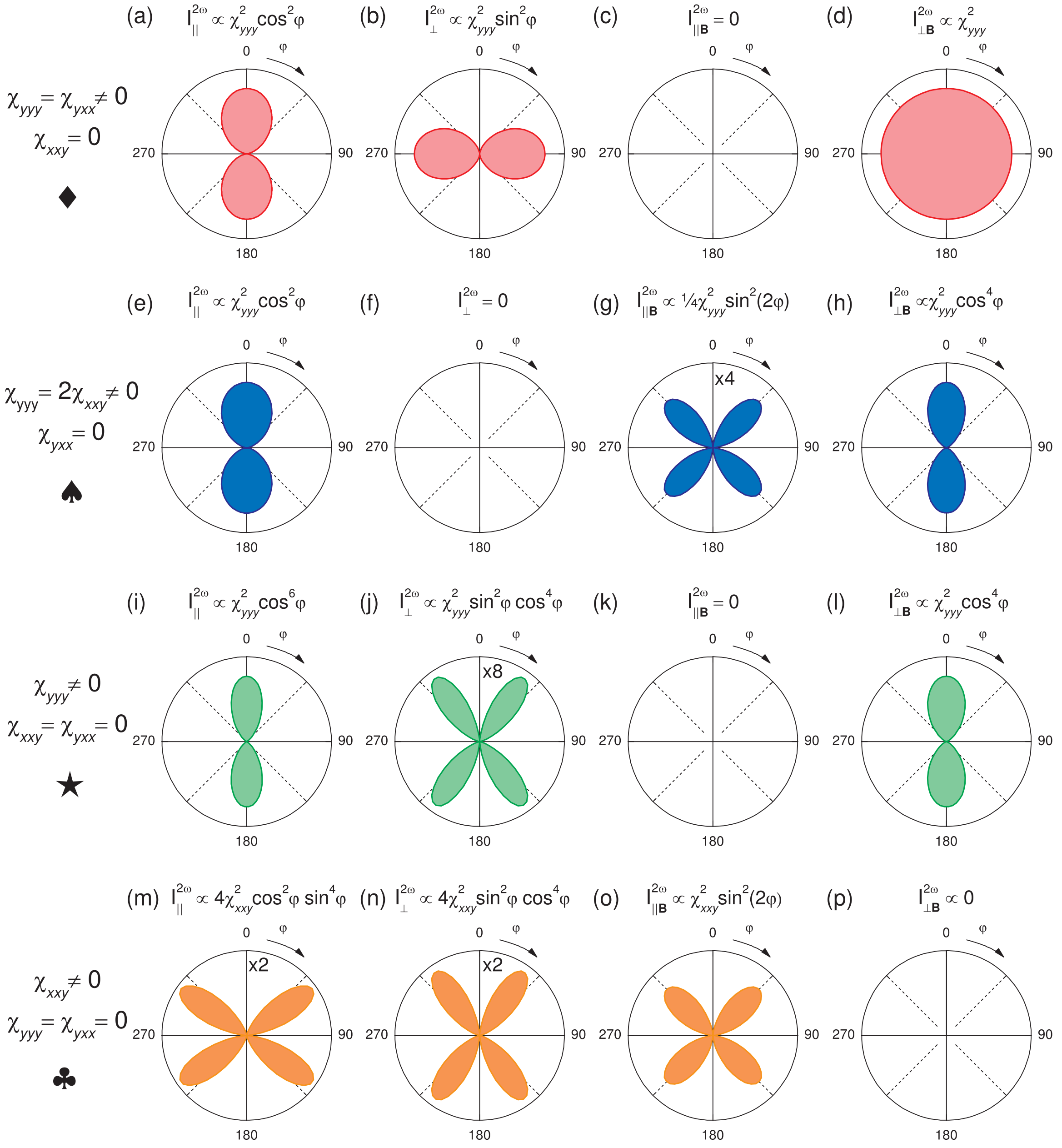

FIG. 16. (Color online) Theoretical predictions for rotational anisotropies of the SHG signal due to different contributions for $I_{\parallel} \mapsto \mathbf{E}^{\omega} \parallel \mathbf{E}^{2\omega}$, $I_{\perp} \mapsto \mathbf{E}^{\omega} \perp \mathbf{E}^{2\omega}$, $I_{\parallel\mathbf{B}} \mapsto \mathbf{E}^{2\omega} \parallel \mathbf{B}$, and $I_{\perp\mathbf{B}} \mapsto \mathbf{E}^{2\omega} \perp \mathbf{B}$ according to Eqs. (8), (10), (7), and (6), respectively, using the relations from Table I: (a)–(d) spin Zeeman effect ♦. (e)–(h) Stark effect / magneto-Stark effect / orbital Zeeman effect ♠. (i)–(l) spin Zeeman effect for $2p_y$ ★. (m)–(p) spin Zeeman effect for $2p_x$ ♣.

$I^{2\omega}_{\perp\mathbf{B}} = 0$. Note that also here the symmetry relation $\chi_{yyy} = \chi_{yxx} + 2\chi_{xxy}$ valid for $6mm$ hexagonal crystal[43] is broken because of the symmetry reduction in the presence of a magnetic-field B_x directed perpendicular to the z axis. This field lifts the degeneracy of the $2p_x$ and $2p_y$ states.

All mechanisms considered above for field-induced SHG at the s and p exciton resonances are summarized in Table I. The susceptibilities are presented for the geometry $\mathbf{k} \parallel \mathbf{z}$, $\mathbf{B} \parallel \mathbf{x}$, and $\mathbf{E} \parallel \mathbf{y}$. Resulting rotational anisotropy patterns corresponding to the different mechanisms are illustrated in Fig. 16.

We have to note, without going into details, that the considered mechanisms do not work in the Faraday geometry $\mathbf{B} \parallel \mathbf{k} \parallel \mathbf{z}$. A magnetic field applied along the hexagonal z axis does not mix the Γ_1 and Γ_5 states, therefore the mechanisms involving Zeeman spin mixing do not induce SHG signals. The orbital Zeeman term $L_z B_z$ also does not lead to admixture of the $2p_z$ states that is allowed for quadrupole emission when $\mathbf{k} \parallel \mathbf{z}$. The effective electric field E_{eff} vanishes for the geometry $\mathbf{B} \parallel \mathbf{k}$, so there is also no magneto-Stark effect.

VI. DISCUSSION

The observed magnetic- and electric-field-induced SHG are specific to excitons, no induced signals are observed in the off-resonant energy range. In the following we discuss the various interactions between light fields and exciton states, leading to the different types of symmetry breaking presented in Sec. V in order to explain our experimental data of Sec. IV. As a general rule, we note that mixing of states with different symmetries is the key factor for inducing resonant nonlinear susceptibilities. Rotational anisotropy measurements of the SHG signals give comprehensive information on the symmetry of the involved nonlinear susceptibilities and, therefore, on the underlying origins. Thus, they help to distinguish different nonlinear optical mechanisms, which is especially important when more than one mechanism becomes involved. Therefore, the measured rotational anisotropy patterns of the SHG intensity should reflect the anisotropies predicted by our theoretical considerations. For the sake of convenience, all discussed states will be referred to as excitons, although states that contain admixtures of s envelope states can couple so strongly to the light field that exciton-polaritons may be formed.

The energy shifts of SHG lines in magnetic field and the field dependence of their intensities should be in accord with the theory as well. The computed energies depend strongly on the input parameters, which are the zero-field exciton energies and the electron and hole effective masses. Here we use the zero-field exciton energies from Refs. 52 and 56: $\mathcal{E}_{2s_{\mathrm{T}}} = 3.4227$ eV, $\mathcal{E}_{2s_{\mathrm{L}}} = 3.4232$ eV, $\mathcal{E}_{2p_z} = 3.4240$ eV, and $\mathcal{E}_{2p_{x,y}} = 3.4254$ eV for the A series as well as $\mathcal{E}_{2s_{\mathrm{T}}} = 3.4276$ eV, $\mathcal{E}_{2s_{\mathrm{L}}} = 3.4304$ eV, $\mathcal{E}_{2p_z} = 3.4292$ eV, and $\mathcal{E}_{2p_{x,y}} = 3.4303$ eV for the B series of excitons. We use the electron effective mass $m_e = 0.27m_0$ and the following hole effective masses obtained from first principles calculations:[44] $m_\parallel = 2.74m_0$, $m_\perp = 0.54m_0$ for the A excitons and $m_\parallel = 3.03m_0$, $m_\perp = 0.55m_0$ for the B excitons. The static dielectric constants $\epsilon_\parallel = 8.49$ and $\epsilon_\perp = 7.40$ are taken from Ref. 77. Spin Zeeman splitting is not included in the calculations for the $2s/2p_z/2p_y$ states. The discussed interactions act on states with the same spin wave functions and thus the spin Zeeman splitting leads to an energy shift, that is the same for all involved states. Therefore, even though the number of lines in Fig. 9 will increase, it should not lead to additional contributions.

A. SHG mechanism for 1s exciton

The SHG signals at the $1s$ exciton resonance can be fully explained by the spin Zeeman effect, mixing one-photon allowed orthoexcitons and two-photon allowed paraexcitons leading to the relations $\chi_{yyy} = \chi_{yxx} \neq 0$ and $\chi_{xxy} = 0$, see Table I and Sec. V C 1. The nonzero component χ_{yyy} given by Eq. (14) predicts the rotational anisotropies shown in Figs. 16(a)–16(d) as well as a quadratic dependence of the SHG intensity on the magnetic field $I^{2\omega} \propto B^2$. The measured intensities $I_\parallel^{2\omega}$ and $I_\perp^{2\omega}$ show indeed the predicted $\cos^2\varphi$ and $\sin^2\varphi$ shape and also have the same amplitude, see Fig. 6(c). Furthermore, no signal was detected for $I_{\parallel\mathbf{B}}^{2\omega}$. $I_{\perp\mathbf{B}}^{2\omega}$ was found to be isotropic (not shown). Figure 7(a) proves the square dependence of $I^{2\omega}$ on the magnetic-field strength. For the $1s(B)$ exciton, which emerges from a different valence band, two SHG mechanisms may be active: (i) mixing of the Γ_5 and Γ_6 states due to the spin Zeeman effect, and (ii) mixing of the A and B valence bands due to exchange interaction.

B. SHG mechanisms for 2s/2p excitons

A similar process based on the magnetic-field-induced spin Zeeman effect, mixing the Γ_5 and Γ_1 states of the $1s(A)$ exciton, is valid also for the $2s(A)$ excitons. However, the comparison of Fig. 6(c) and Figs. 10(a) and 10(b) shows that the observed anisotropies of the $n = 2$ signals are different from those of the $1s$ states: For the $n = 2\,(A)$ excitons the shape of $I_\perp^{2\omega}$ cannot be described by the form $\sin^2\varphi$, and $I_\parallel^{2\omega}$ and $I_\perp^{2\omega}$ do not have the same amplitude. These anisotropies need to be explained by other mechanisms than the spin Zeeman effect on the s envelope.

In Ref. 76 we have shown that the magneto-Stark effect is the dominant mechanism in the $2s/2p(A,B)$ exciton region. It can explain the shapes shown in Figs. 10(a), 10(c), and 10(d), which closely resemble the predicted shapes in Figs. 16(e), 16(g), and 16(h), respectively. But a closer look at the nonvanishing $I_\perp^{2\omega}$ intensity reveals that the spin Zeeman effect on both the s and p envelopes add a small contribution, note the multiplication factor 20 in Fig. 10(b). The complex shape of $I_\perp^{2\omega}$ in Fig. 10(b) can only be explained by a combination of the spin Zeeman effects on the $n = 2$ states. Their predicted shapes are shown in Figs. 16(b) and 16(j), respectively. To compare their impact, Figs. 10 and 11 give their ratio a/b. a and b describe the relative strength of the spin Zeeman effect on the s and p_y envelope, respectively. Both contributions to $I_\perp^{2\omega}$ can be estimated to be of about 5% of the peak intensity of $I_\parallel^{2\omega}$, while it follows from the fit in Fig. 10(b) that the spin Zeeman contribution from the $2p_y(A)$ part is twice as strong as from the $2s(A)$ part. As a consequence, the SHG induced by the magneto-Stark effect involving only ED excitation as well as ED emission processes is about 40 times more efficient than the SHG due to the spin Zeeman mixing utilizing a MD transition.

The orbital Zeeman effect cannot be distinguished from the magneto-Stark effect via anisotropies (see nonzero components of both contributions in Table I) and might be of importance too, due to the $2p_y/2p_z$ mixing, especially for the regions where the $2p_z$ part is large. However, the probability of MD emission from the $2p_z$ part is very low in comparison with the probability of ED emission from the $2s$ state. Thus we assume that the orbital Zeeman effect does not play a leading role and the magneto-Stark effect brings the dominant contribution to the SHG signal at the $2s/2p$ exciton resonances.

Furthermore, the weak nonzero signals in the crossed geometry that do not follow from the magneto-Stark effect were also observed in the range of the $n = 2(B)$ excitons. The anisotropy shapes for the B series presented in Figs. 11(a), 11(b), 11(e), and 11(f) show many similarities to those of the A series: The strongest signals are observed for $I_\parallel^{2\omega}$ with a twofold $\cos^2\varphi$ symmetry pattern, whereas $I_\perp^{2\omega}$ is a mixture of a fourfold $\sin^2\varphi\cos^4\varphi$ and a twofold $\sin^2\varphi$ pattern, originating from the spin Zeeman effects. In addition, the contribution $I_\perp^{2\omega} \propto \sin^2\varphi$ in the range of the $n = 2$ B exciton energies might also arise from the spin Zeeman effect on the $3s(A)$ or $1s(C)$ excitons, located in the same spectral range. However, the $3s(A)$ contribution is rather unlikely, because of the high main quantum number considerably reduces its oscillator strength in comparison to $1s$ and $2s$ states. By contrast, the $1s(C)$ is also seen as a strong, broad feature in the crystallographic SHG spectra, see Fig. 3. Actually an additional contribution from the $1s(C)$ exciton would explain why we observed a strong influence of the s-type spin Zeeman effect on the shape of the anisotropies for $2\hbar\omega = 3.432$ eV; see Figs. 11(e) and 11(f). Only in this region the ratio a/b is larger than 1. Furthermore, the magneto-Stark effect is not as important as for the other energies; compare the ratios $I^{2\omega}_{\parallel}/I^{2\omega}_{\perp}$ at the three energies shown in Fig. 11.

The strongest SHG signals are observed for $I^{2\omega}_{\parallel}$ and their spectral maxima follow the energies of the states with dominant $2p_y(A,B)$ wave functions. In higher fields (>6 T) the peaks follow lines with dominant $2s$ wave functions, because the admixture of the $2p_z$ to $2p_y$ states reduces the efficiency of the magneto-Stark induced SHG; see the blue circles in Fig. 9. The analysis of the anisotropies in the regions where the $2p_y/2p_z$ wave functions dominate gives the same results as the analysis of states with large $2s$ contributions, but with less influence from the s-type spin Zeeman effect. Consequently, the SHG at the $2s/2p_y/2p_z$ states is governed mainly by the magneto-Stark effect.

The contributions from the spin Zeeman effect on the $2p_x$ states are best seen in Fig. 8 for $I^{2\omega}_{\parallel\mathbf{B}}$ in the geometry $\varphi(\mathbf{E}^{\omega}) = 45^{\circ}$ and $\mathbf{E}^{2\omega} \parallel \mathbf{B}$. The spectral maxima follow the calculated energies of the $2p_x(A,B)$ exciton states; compare $2p_x$ lines and red circles in Fig. 9. In addition, the ratio of the spectrally integrated intensities $I^{2\omega}_{\parallel\mathbf{B}}/I^{2\omega}_{\parallel}$ should be $1/4$ or less without the contribution of the spin Zeeman effect for the $2p_x$ states. We observed, however, a deviating ratio of about $1/3$ [compare area under curves in Fig. 8(b)], underlining the importance of the spin Zeeman mechanism for the $2p_x$ orbitals oriented parallel to the magnetic field. Nevertheless, the contributions of this mechanism to the $I^{2\omega}_{\parallel}$ signals are not significant and most of the integrated SHG intensity in the $I^{2\omega}_{\parallel\mathbf{B}}$ spectra comes from the $2s/2p_y/2p_z$ mixed states due to the magneto-Stark effect.

The developed model describes well the measured angular dependences of the SHG intensities and it is in reasonable accordance with the energy shifts of the exciton states shown in Fig. 9, ensuring the validity of the presented SHG mechanisms.

Another intriguing feature of the discovered mechanisms is the complex behavior of the spectrally integrated SHG intensity shown in Fig. 7(b). The SHG signals from the magneto-Stark and orbital Zeeman effects are expected to saturate when the related energies become larger than the zero-field splitting of the involved exciton states. The typical values of the $|2s_{\mathrm{T}} - 2p_y|$ exciton splitting is about 3 meV for the A and B excitons in ZnO. While the longitudinal-transversal splitting of the $2s(A)$ exciton is about 0.5 meV, the respective splitting for the B exciton is about 3 meV. Thus, the saturation condition is reached for the orbital Zeeman effect ($g_{\mathrm{orb}}\mu_{\mathrm{B}}B_x$) around $B \approx 8$ T, but it is not fulfilled for the magneto-Stark effect [$3eE_{\mathrm{eff}}(B)a_{\mathrm{B}}$] even at the strongest field of $B \leqslant 10$ T. The spin Zeeman effect for the $2p_x$ state is independent of magnetic field, whereas the susceptibility decreases with the fraction of C_{2p_y}, as for the $2p_y$ state, compare Eq. (17). Due to the linewidths of the exciton resonances, we were not able to resolve in Fig. 8 individual lines, but rather the interplay of contributions from different energies leading to the observed complex behavior of the spectrally integrated intensity. For the geometry shown in Fig. 7(b) we take into account the magneto-Stark and orbital Zeeman effects to model the SHG intensity dependence. The model calculation for the strongest peak $2\hbar\omega = 3.4254$ eV reproduces well the observed dependence, assuming $\Gamma = 1.2$ meV and $\chi^{\text{magneto-Stark}} : \chi^{\text{orbital Zeeman}} \approx 100:1$. Slight deviations can be expected, as in the experiment the data were spectrally integrated. If the spin Zeeman effect is taken into account the model calculations lead to a dependence with a shoulder, shown for $\mathbf{E}^{2\omega} \parallel \mathbf{E}^{\omega} \perp \mathbf{B}$ in Ref. 76.

C. Temperature dependence

The temperature dependence of the integrated SHG intensity can be qualitatively understood by a simple consideration. Equation (4) shows that the susceptibility for resonant SHG depends inversely linear on the exciton damping Γ_{exc}, which is contributed by inhomogeneous and homogeneous broadening of the exciton. The inhomogeneous broadening in the studied sample does not exceed 1 meV, one can see that in Fig. 6(a), where it is already limited by the laser spectral width. Therefore, at temperatures exceeding 10–20 K the exciton linewidth is controlled by the homogeneous broadening due to scattering on acoustic phonons. This broadening increases linearly with the temperature. The SHG peak intensity, proportional to the susceptibility, depends inversely quadratically on the linewidth $I^{2\omega} \propto \Gamma_{\mathrm{exc}}^{-2}$. The dependences for the exciton resonances in Fig. 14 are spectrally integrated, for which the intensities in principle have to be multiplied with the linewidth leading to the integrated SHG being proportional to $\Gamma_{\mathrm{exc}}^{-1}$ and respectively to T^{-1}. In contrast, the crystallographic SHG signal measured in the off-resonant region remains constant with increasing temperature, compare blue and red curves in the lower energy region in Fig. 13.

D. Origin of X line

To our knowledge the observed strong SHG line at 3.407 eV has not been reported in linear absorption spectra studies. However, the observed temperature and angular dependences of the SHG at this line correspond to those of the free $1s(C)$ exciton; compare Figs. 4(b) and 4(d). Thus, a correlation between these resonances is likely. In addition, we want to point out the recent observation of an unknown line at $\sim$3.405 eV with polarization pattern and uniaxial pressure coefficients matching those of the $C_T(\Gamma_1)$ state,[78] suggesting to link the X line to the C valence band. Suggesting that the X line is the bound state of $1s(C)$ exciton shifted to lower energy by 26 meV, one may expect to observe such resonances below $1s(A)$ and $1s(B)$ excitons as well. However, we did not find resonances at the corresponding energies for the A and B excitons. Clarification of the X-line origin needs further investigations. We also note that phase synchronization for the fundamental and second-harmonic waves are of great importance for SHG. Therefore, the strong SHG line at 3.407 eV might be due to phase matching[29] as consequence of polaritonic effects in the dielectric function in the exciton energy range[53] of ZnO.

E. Crossed electric and magnetic fields

To verify the magneto-Stark effect as a dominant source of the observed SHG signals, it is instructive to discuss the joint action of external magnetic and electric fields. Theory predicts that an electric field produces the same type of symmetry breaking as the effective electric field induced by a magnetic field. This is proven by the fact that the anisotropy of magnetic-field-induced signals is not changed by additionally applying an electric field. Nevertheless, the electric field acts very differently in comparison to the magnetic field. The effective electric field acts on exciton levels only, whereas the electric field creates a potential throughout the crystal.

Figure 15(b) shows that an electric field of 550 V/cm has only a weak effect on the SHG intensity. The interference of its action with the effective electric field induced by a magnetic field of 1 T in Fig. 15(a) shows that the electric field gives indeed surprisingly small contributions. The magnitude of the effective electric field is $E_{\text{eff}} = \frac{\hbar}{M_{\text{exc}}} k_{\text{exc}} B_x$. The theoretical value for the exciton effective mass in ZnO is about $3m_0$[44] and $k_{\text{exc}} = n\mathcal{E}_{\text{exc}}/\hbar c \approx 0.03\ \text{nm}^{-1}$ for $\mathcal{E}_{\text{exc}} = 3.425$ eV with a refractive index $n \approx 1.97$.[77,79] Thus, E_{eff} can be estimated as ≈ 12 V/cm for $B = 1$ T. Consequently, the ratio between the effective electric field and the electric field strength giving the same effect is $\gamma = \frac{1}{12[\text{V/cm}]\epsilon_\perp} \approx 1.13 \times 10^{-2}$ T/V (where $\epsilon_\perp$ is the relative dielectric permittivity) and would have to be used for the fit function $I^{2\omega} \propto (\pm B \pm \gamma E)^2$. Instead the best fit to the data shown in the inset of Fig. 15(a) was achieved for a value that is 50 times smaller. Such a discrepancy evidences that much weaker electric field is in fact acting on the excitons in our experiments. Indeed, as it is shown in Fig. 15(c), the sample resistivity was reduced drastically when the $2\hbar\omega$ of the laser light approaches $2p$ states and after illumination the resistivity is only slowly restored. We suggest that the screening of the external field by carriers trapped in deep centers is responsible for the observed discrepancy.

VII. CONCLUSIONS

In summary, new exciton phenomena in bulk hexagonal ZnO have been thoroughly studied by optical second-harmonic generation in the spectral range of the $1s(A,B)$, $2s(A,B)$, $2p(A,B)$, and $1s(C)$ excitons, both experimentally and theoretically. While symmetry considerations forbid any crystallographic SHG for $\mathbf{k} \parallel \mathbf{z}$, strong magnetic-field-induced contributions are found for this geometry. Novel microscopic mechanisms for these nonlinearities are identified and confirmed by detailed experimental studies, addressing the magnetic field, electric field, temperature, and polarization dependences of the SHG signals.

We present an in-depth theoretical analysis on the basis of phenomenological and microscopic approaches, which suggests several mechanisms induced by external magnetic field. The magnetic field produces a multifaceted action, depending on the exciton type. The nonlinear mechanisms are related to the spin and orbital Zeeman effects, and to the magneto-Stark effect. For $1s(A,B)$ excitons the main mechanism of magnetic-field-induced SHG is related to the spin Zeeman effect, which mixes the different spin wave functions. On the other hand, the mixing of envelope wave functions of opposite parity by the magneto-Stark effect due to an effective electric field is the key mechanism for magnetic-field-induced SHG at the closely spaced $2s/2p(A,B)$ excitons. The role of the orbital Zeeman effect for mixing of the $2p_z$ and $2p_y$ orbitals and the spin Zeeman effect on the $2p_x$ and $2p_y$ spin wave functions has been also discussed. Application of an external electric field gives rise to the Stark effect enabling SHG by mixing the wave functions of the $2s/2p(A,B)$ excitons.

We show the key importance of magnetic- and electric-field-induced symmetry reductions for inducing nonlinearities in bulk hexagonal ZnO, a phenomenon which should occur in the same way also for other material systems. Tailoring these symmetry reductions of the exciton level structure opens new degrees of freedom in the nonlinear spectroscopy of excitons.

ACKNOWLEDGMENTS

The authors are thankful to D. Fröhlich for highly stimulating discussions and help with experiments, to E. L. Ivchenko for discussions, and to B. Kaminski for his contribution to the initial stage of this study. This work was supported by the Deutsche Forschungsgemeinschaft, the Russian Foundation for Basic Research and the Goverment of Russia through the program P220 (project 14.B25.31.0025, leading scientist A. K. Tagantsev). A.V.R. is grateful for the financial support received from the Swiss National Science Foundation. V.V.P. research stay in Dortmund was supported by the Alexander-von-Humboldt Foundation.

APPENDIX: THEORETICAL CONSIDERATION OF EXCITON STATE MIXING IN ELECTRIC AND MAGNETIC FIELDS

Here we describe the mixed exciton states in hexagonal ZnO subject to external electric or magnetic fields. Only the geometry used in the experimental part of this paper is analyzed: $\mathbf{k} \parallel \mathbf{z}$, $\mathbf{E} = (0,E_y,0)$, and $\mathbf{B} = (B_x,0,0)$.

1. Exciton states in electric field perpendicular to hexagonal z axis

The external electric field E_y mixes the $2s$ and $2p_y$ exciton states of opposite parity for the A and B exciton series, but does not affect their spin states. We neglect for simplicity the interaction between the A and B series and consider them independently within the polariton concept. Then for each series the exciton eigenenergies in the external field E_y and the mixed exciton functions can be found from diagonalization of the Hamiltonian

$$\hat{H}_{2s/2p_y} = \begin{pmatrix} \mathcal{E}_{2s} & 3eE_y a_{\text{B}} \\ 3eE_y a_{\text{B}} & \mathcal{E}_{2p_y} \end{pmatrix}, \tag{A1}$$

where a_{B} is the exciton Bohr radius, $\mathcal{E}_{2s} = \mathcal{E}_{2s_{\text{T}}}$ is the zero-field energy of the $2s$ transversal exciton, and $\mathcal{E}_{2p_y}$ is that of the $2p_y$ exciton state. The eigenenergies are

$$\mathcal{E}^{\pm}_{2s_{\text{T}}/2p_y} = \frac{1}{2}\left[\mathcal{E}_{2s_{\text{T}}} + \mathcal{E}_{2p_y} \pm \sqrt{\left(\mathcal{E}_{2p_y} - \mathcal{E}_{2s_{\text{T}}}\right)^2 + 36(eE_y a_{\text{B}})^2}\right], \tag{A2}$$

and the resulting wave functions can be written as

$$\Psi_{2s_{\mathrm{T}}/2p_y} = C_{2s_{\mathrm{T}}}(E_y)\Psi_{2s} + C_{2p_y}(E_y)\Psi_{2p_y}, \tag{A3}$$

with

$$C_{2s_{\mathrm{T}}}(E_y) = \frac{\mathcal{E}_{2p_y} - \mathcal{E}^{\pm}_{2s_{\mathrm{T}}/2p_y}}{\sqrt{(3eE_y a_{\mathrm{B}})^2 + \left(\mathcal{E}_{2p_y} - \mathcal{E}^{\pm}_{2s_{\mathrm{T}}/2p_y}\right)^2}}, \tag{A4}$$

$$C_{2p_y}(E_y) = -\frac{3eE_y a_{\mathrm{B}}}{\sqrt{(3eE_y a_{\mathrm{B}})^2 + \left(\mathcal{E}_{2p_y} - \mathcal{E}^{\pm}_{2s_{\mathrm{T}}/2p_y}\right)^2}}. \tag{A5}$$

In the considered geometry these exciton states are transversal excitons. Due to interaction with the light field two transversal polariton branches for each of the $2s/2p_y$ mixed states are formed. The energies of the lower polariton branches are given by Eq. (A2). To find the energies of the upper polariton branches one has to consider the interaction of the mixed excitons with photons and their corresponding contribution to the dielectric function. However, when the longitudinal-transversal splitting $\Delta^{2s}_{\mathrm{LT}}$ is much smaller than all characteristic energies, the results can be approximated by considering the direct interaction between the $2p_y$ exciton and the upper $2s$ polariton branch. For this, one has to use the $\mathcal{E}_{2s} = \mathcal{E}_{2s_{\mathrm{L}}}$ in the Hamiltonian (A1). The resulting energies of the upper polariton branches (UPB) are approximately given by

$$\mathcal{E}^{\pm}_{2s_{\mathrm{L}}/2p_y} \approx \frac{1}{2}\left[\mathcal{E}_{2s_{\mathrm{L}}} + \mathcal{E}_{2p_y} \pm \sqrt{\left(\mathcal{E}_{2p_y} - \mathcal{E}_{2s_{\mathrm{L}}}\right)^2 + 36(eE_y a_{\mathrm{B}})^2}\right], \tag{A6}$$

where $\mathcal{E}_{2s_{\mathrm{L}}} = \mathcal{E}_{2s_{\mathrm{T}}} + \Delta^{2s}_{\mathrm{LT}}$ is the energy of the $2s$-longitudinal exciton and the upper polariton in zero electric field. The resulting wave functions can be found using Eqs. (A2)–(A5) after replacing the energy $\mathcal{E}_{2s_{\mathrm{T}}}$ with $\mathcal{E}_{2s_{\mathrm{L}}}$.

2. 1*s* excitons in external magnetic field perpendicular to hexagonal *z* axis

The spin states of the A and C $1s$ excitons are formed from the conduction band of Γ_7 symmetry and the valence band of Γ_7 symmetry and thus can be of Γ_5, Γ_1, or Γ_2 symmetry, split from each other by the electron-hole exchange interaction. The external magnetic-field B_x mixes the Γ_{5y} and Γ_1 spin states. The resulting SHG active states can be found from the Hamiltonian

$$\hat{H}_{\Gamma_{5y}/\Gamma_1} = \begin{pmatrix} \mathcal{E}_{\Gamma_1} & \mu_{\mathrm{B}} g_{\mathrm{exc}} B_x/2 \\ \mu_{\mathrm{B}} g_{\mathrm{exc}} B_x/2 & \mathcal{E}_{\Gamma_5} \end{pmatrix}, \tag{A7}$$

where $\mathcal{E}_{\Gamma_1}$ and $\mathcal{E}_{\Gamma_5}$ are the zero-field energies of the corresponding states, and $g_{\mathrm{exc}} = (g^{\perp}_{\mathrm{h}} - g^{\perp}_{\mathrm{e}})$ is the g factor of the $1s$ state for $\mathbf{B} \perp \mathbf{k}$. In ZnO, for the A exciton $g^{\perp}_{\mathrm{e}} \approx 1.95$ and $g^{\perp}_{\mathrm{h}} \approx 0$.[44] The resulting energies of the $1s(A)$ states in magnetic-field B_x are given by

$$\mathcal{E}^{\pm}_{\Gamma_{5y}/\Gamma_1} = \tfrac{1}{2}\left[\mathcal{E}_{\Gamma_1} + \mathcal{E}_{\Gamma_5} \pm \sqrt{\Delta^2_{15} + (\mu_{\mathrm{B}} g_{\mathrm{exc}} B_x)^2}\right], \tag{A8}$$

where $\Delta_{15} = |\mathcal{E}_{\Gamma_5} - \mathcal{E}_{\Gamma_1}|$ is the exchange splitting. The LPB is described exactly by Eq. (A8) with energy $\mathcal{E}_{\Gamma_5} = \mathcal{E}_{1s_{\mathrm{T}}}$, the UPB is described approximately by Eq. (A8) with energy $\mathcal{E}_{\Gamma_5} = \mathcal{E}_{1s_{\mathrm{L}}}$. The resulting wave functions are given by

$$\Psi_{\Gamma_5/\Gamma_1} = C_{\Gamma_5}(B_x)\Psi_{\Gamma_5} + C_{\Gamma_1}(B_x)\Psi_{\Gamma_1}, \tag{A9}$$

with

$$C_{\Gamma_5}(B_x) = \frac{2\left(\mathcal{E}_{\Gamma_5} - \mathcal{E}^{\pm}_{\Gamma_{5y}/\Gamma_1}\right)}{\sqrt{(\mu_{\mathrm{B}} g_{\mathrm{exc}} B_x)^2 + 4\left(\mathcal{E}_{\Gamma_5} - \mathcal{E}^{\pm}_{\Gamma_{5y}/\Gamma_1}\right)^2}}, \tag{A10}$$

$$C_{\Gamma_1}(B_x) = -\frac{\mu_{\mathrm{B}} g_{\mathrm{exc}} B_x}{\sqrt{(\mu_{\mathrm{B}} g_{\mathrm{exc}} B_x)^2 + 4\left(\mathcal{E}_{\Gamma_5} - \mathcal{E}^{\pm}_{\Gamma_{5y}/\Gamma_1}\right)^2}}. \tag{A11}$$

3. 2*s* and 2*p* exciton states in magnetic field perpendicular to hexagonal *z* axis

Similar to the effect of the external electric field E_y considered above, the effective electric field $E_{\mathrm{eff}} = \frac{\hbar}{M_{\mathrm{exc}}} k_{\mathrm{exc}} B_x$ that originates from the magneto-Stark effect [see Eq. (13)], mixes the $2s$ and $2p_y$ excitons of opposite parity. At the same time, the Zeeman orbital effect mixes the $2p_z$ and $2p_y$ states of the same parity. The resulting energies $\mathcal{E}^{i}_{2s/2p_z/2p_y}$ ($i =$ 1,2,3 label eigenvalues) of the mixed $2s/2p_z/2p_y$ polariton branches can be found as the eigenenergies of the Hamiltonian

$$\hat{H}^{\pm}_{2s/2p_z/2p_y} = \begin{pmatrix} \mathcal{E}^{\pm}_{2s}(B_x) & 0 & 3eE_{\mathrm{eff}} a_{\mathrm{B}} \\ 0 & \mathcal{E}^{\pm}_{2p_z}(B_x) & i g_{\mathrm{orb}} \mu_{\mathrm{B}} B_x \\ 3eE_{\mathrm{eff}} a_{\mathrm{B}} & -i g_{\mathrm{orb}} \mu_{\mathrm{B}} B_x & \mathcal{E}^{\pm}_{2p_y}(B_x) \end{pmatrix}. \tag{A12}$$

Here

$$\mathcal{E}^{\pm}_{2s}(B_x) = E_{2s} + 14 C_d B_x^2 \pm \mu_{\mathrm{B}} g^{\perp}_{\mathrm{e}} B_x/2, \tag{A13}$$

$$\mathcal{E}^{\pm}_{2p_z}(B_x) = \mathcal{E}_{2p_z} + 12 C_d B_x^2 \pm \mu_{\mathrm{B}} g^{\perp}_{\mathrm{e}} B_x/2, \tag{A14}$$

$$\mathcal{E}^{\pm}_{2p_y}(B_x) = \mathcal{E}_{2p_y} + 12 C_d B_x^2 \pm \mu_{\mathrm{B}} g^{\perp}_{\mathrm{e}} B_x/2, \tag{A15}$$

where C_d describes the diamagnetic shift, and g_{orb} is the orbital g factor. Expressions for C_d and g_{orb} can be found, for example, in Ref. 45. We assume the electron-hole short-range exchange splitting to be zero for all $2s$ and $2p$ states and $g^{\perp}_{h} = 0$, so that all states are additionally two times degenerate with respect to the hole spin projection.

Accounting for the different spin states and polariton branches one has to deal with 24 mixed polariton states of the A exciton and 24 mixed polariton states of the B exciton. However, the perturbations in Hamiltonian (A12) mix only the states belonging to the same spin states and the same polariton branches. Therefore, in fact one has to consider only the magnetic-field-induced mixing of the envelopes. Then the energies $\mathcal{E}^{i}_{2s_{\mathrm{T}}/2p_z/2p_y}$ of the LPB mixed states and $\mathcal{E}^{i}_{2s_{\mathrm{L}}/2p_z/2p_y}$ of the UPB mixed states can be calculated as roots of the following equation:

$$\begin{aligned}&(\mathcal{E}^i - \mathcal{E}^{\pm}_{2s})\left(\mathcal{E}^i - \mathcal{E}^{\pm}_{2p_z}\right)\left(\mathcal{E}^i - \mathcal{E}^{\pm}_{2p_y}\right) - (3eE_{\mathrm{eff}} a_{\mathrm{B}})^2\left(\mathcal{E}^i - \mathcal{E}^{\pm}_{2p_z}\right)\\ &\quad -(g_{\mathrm{orb}} \mu_{\mathrm{B}} B_x)^2(\mathcal{E}^i - \mathcal{E}^{\pm}_{2s}) = 0,\end{aligned} \tag{A16}$$

with $\mathcal{E}_{2s} = \mathcal{E}_{2s_{\mathrm{T}}}$ for the LPB and $\mathcal{E}_{2s} = \mathcal{E}_{2s_{\mathrm{L}}}$ for the UPB.

The resulting wave functions for the $2s/2p_z/2p_y$ mixed states contain all three components

$$\Psi^{i}_{2s/2p_z/2p_y} = C^{i}_{2s}(B_x)\Psi_{2s} + C^{i}_{2p_z}(B_x)\Psi_{2p_z} + C^{i}_{2p_y}(B_x)\Psi_{2p_y}, \tag{A17}$$

with the coefficients

$$C^i_{2s} = \frac{3eE_{\text{eff}}a_{\text{B}}\left(\mathcal{E}^i - \mathcal{E}^{\pm}_{2p_z}\right)}{\sqrt{(\mathcal{E}^i - \mathcal{E}^{\pm}_{2s})^2\left(\mathcal{E}^i - \mathcal{E}^{\pm}_{2p_z}\right)^2 + (3eE_{\text{eff}}a_{\text{B}})^2\left(\mathcal{E}^i - \mathcal{E}^{\pm}_{2p_z}\right)^2 + (g_{\text{orb}}\mu_{\text{B}}B_x)^2(\mathcal{E}^i - \mathcal{E}^{\pm}_{2s})^2}}, \tag{A18}$$

$$C^i_{2p_z} = \frac{i g_{\text{orb}}\mu_{\text{B}}B_x(\mathcal{E}^i - \mathcal{E}^{\pm}_{2s})}{\sqrt{(\mathcal{E}^i - \mathcal{E}^{\pm}_{2s})^2\left(\mathcal{E}^i - \mathcal{E}^{\pm}_{2p_z}\right)^2 + (3eE_{\text{eff}}a_{\text{B}})^2\left(\mathcal{E}^i - \mathcal{E}^{\pm}_{2p_z}\right)^2 + (g_{\text{orb}}\mu_{\text{B}}B_x)^2(\mathcal{E}^i - \mathcal{E}^{\pm}_{2s})^2}}, \tag{A19}$$

$$C^i_{2p_y} = \frac{(\mathcal{E}^i - \mathcal{E}^{\pm}_{2s})\left(\mathcal{E}^i - \mathcal{E}^{\pm}_{2p_z}\right)}{\sqrt{(\mathcal{E}^i - \mathcal{E}^{\pm}_{2s})^2\left(\mathcal{E}^i - \mathcal{E}^{\pm}_{2p_z}\right)^2 + (3eE_{\text{eff}}a_{\text{B}})^2\left(\mathcal{E}^i - \mathcal{E}^{\pm}_{2p_z}\right)^2 + (g_{\text{orb}}\mu_{\text{B}}B_x)^2(\mathcal{E}^i - \mathcal{E}^{\pm}_{2s})^2}}. \tag{A20}$$

It is worth to note that the Hamiltonian (A12) allows one to take into account the effects of both the external magnetic-field B_x and the external electric field E_y. For that purpose, E_{eff} should be replaced with $E_{\text{eff}} \pm E_y$, where the choice of the sign depends on the direction of the applied electric field.

The magnetic-field B_x affects the $2p_x$ exciton state only via the spin Zeeman effect and the diamagnetic shift, but does not mix it with the other $2p$ or $2s$ states. Its energy is given by

$$\mathcal{E}^{\pm}_{2p_x}(B_x) = \mathcal{E}_{2p_x} + 6C_d B_x^2 \pm \mu_{\text{B}} g_{\text{e}}^{\perp} B_x/2. \tag{A21}$$

It is important to note, however, that the degeneracy of the $2p_x$ and $2p_y$ states is lifted by the magnetic field and the hexagonal symmetry is broken, i.e., $\chi_{yyy} = \chi_{yxx} + 2\chi_{xxy}$ is violated for these states.

[1] N. Bloembergen, *Nonlinear Optics, Lecture Notes* (W. A. Benjamin, New York, 1965).

[2] Y. R. Shen, *The Principles of Nonlinear Optics* (Wiley, New York, 2003).

[3] R. W. Boyd, *Nonlinear Optics*, 3rd ed. (Academic/Elsevier, Burlington, 2008).

[4] M. Bass (ed.), *Handbook of Optics*, Vol. IV, Optical Properties of Materials, Nonlinear Optics, Quantum Optics, 3rd ed. (McGraw Hill, New York, 2010).

[5] D. N. Nikogosyan, *Nonlinear Optical Crystals: A Complete Survey* (Springer Science and Business Media, New York, 2005).

[6] M. Fiebig, V. V. Pavlov, and R. V. Pisarev, J. Opt. Soc. Am. **22**, 96 (2005).

[7] R. V. Pisarev, B. Kaminski, M. Lafrentz, V. V. Pavlov, D. R. Yakovlev, and M. Bayer, Phys. Status Solidi B **247**, 1498 (2010).

[8] R. V. Pisarev, J. Lumin. **133**, 169 (2013).

[9] E. Garmire, Am. J. Phys. **79**, 245 (2011).

[10] E. Garmire and A. Kost (eds.), *Nonlinear Optics in Semiconductors* (Academic, New York, 1999), Vols. I and II.

[11] H. P. Wagner, M. Kühnelt, W. Langbein, and J. M. Hvam, Phys. Rev. B **58**, 10494 (1998).

[12] See, for example, S. Bergfeld and W. Daum, Phys. Rev. Lett. **90**, 036801 (2003), and references therein.

[13] R. C. Miller, Appl. Phys. Lett. **5**, 17 (1964).

[14] G. Wang, G. K. L. Wong, and J. B. Ketterson, Appl. Opt. **40**, 5436 (2001).

[15] G. Wang, G. T. Kiehne, G. K. L. Wong, J. B. Ketterson, X. Liu, and R. P. H. Chang, Appl. Phys. Lett. **80**, 401 (2002).

[16] M. Abe, N. Awata, T. Matsushita, M. Hakamata, K. Ozawa, R. Murakami, I. Shoji, and T. Kondo, J. Opt. Soc. Am. B **29**, 2392 (2012).

[17] X. Q. Zhang, Z. K. Tang, M. Kawasaki, A. Ohtomo, and H. Koinuma, J. Phys.: Condens. Matter **15**, 5191 (2003).

[18] G. A. Medvedkin and V. G. Voevodin, J. Opt. Soc. Am. **22**, 1884 (2005).

[19] V. Kumar, S. K. Tripathy, and V. Jha, Appl. Phys. Lett. **101**, 192105 (2012).

[20] E. K. Chang, E. L. Shirley, and Z. H. Levine, Phys. Rev. B **65**, 035205 (2001).

[21] R. Leitsmann, W. G. Schmidt, P. H. Hahn, and F. Bechstedt, Phys. Rev. B **71**, 195209 (2005).

[22] T. G. Pedersen and H. D. Cornean, Eur. Phys. Lett. **78**, 27005 (2007).

[23] F. Minami, K. Inoue, Y. Kato, K. Yoshida, and K. Era, Phys. Rev. Lett. **67**, 3708 (1991).

[24] F. Minami, Y. Mitsumori, and S. Matsushita, Phys. Status Solidi B **202**, 775 (1997).

[25] M. Y. Shen, S. Koyama, M. Saito, T. Goto, and N. Kuroda, Phys. Rev. B **53**, 13477 (1996).

[26] S. Kono and N. Nagasawa, J. Lumin. **76-77**, 86 (1998).

[27] C. Schweitzer, D. Fröhlich, K. Reimann, P. Prystawko, M. Leszczynski, and T. Suski, Mater. Sci. Eng. B **82**, 156 (2001).

[28] D. C. Haueisen and H. Mahr, Phys. Rev. Lett. **26**, 838 (1971).

[29] D. C. Haueisen and H. Mahr, Phys. Rev. B **8**, 734 (1973).

[30] A.-M. Janner, R. Eder, B. Koopmans, H. T. Jonkman, and G. A. Sawatzky, Phys. Rev. B **52**, 17158 (1995).

[31] A.-M. Janner, H. T. Jonkman, and G. A. Sawatzky, Phys. Rev. B **63**, 085111 (2001).

[32] V. V. Pavlov, A. M. Kalashnikova, R. V. Pisarev, I. Sänger, D. R. Yakovlev, and M. Bayer, Phys. Rev. Lett. **94**, 157404 (2005).

[33] I. Sänger, D. R. Yakovlev, B. Kaminski, R. V. Pisarev, V. V. Pavlov, and M. Bayer, Phys. Rev. B **74**, 165208 (2006).

[34] I. Sänger, D. R. Yakovlev, R. V. Pisarev, V. V. Pavlov, M. Bayer, G. Karczewski, T. Wojtowicz, and J. Kossut, Phys. Rev. Lett. **96**, 117211 (2006).

[35] B. Kaminski, M. Lafrentz, R. V. Pisarev, D. R. Yakovlev, V. V. Pavlov, V. A. Lukoshkin, A. B. Henriques, G. Springholz, G. Bauer, E. Abramof, P. H. O. Rappl, and M. Bayer, Phys. Rev. Lett. **103**, 057203 (2009).

[36] B. Kaminski, M. Lafrentz, R. V. Pisarev, D. R. Yakovlev, V. V. Pavlov, V. A. Lukoshkin, A. B. Henriques, G. Springholz, G. Bauer, E. Abramof, P. H. O. Rappl, and M. Bayer, Phys. Rev. B **81**, 155201 (2010).

[37] C. Klingshirn, Phys. Status Solidi B **244**, 3027 (2007).

[38] Ü. Özgür, Ya. I. Alivov, C. Liu, A. Teke, M. A. Reshchikov, S. Doğan, V. Avrutin, S.-J. Cho, and H. Morkoç, J. Appl. Phys. **98**, 041301 (2005).

[39] H. Landolt and R. Börnstein, in *Numerical Data and Functional Relationship in Science and Technology*, New Series III Vols. 17B, 22, and 41B, edited by U. Rösler *et al.* (Springer, Berlin, 1999).

[40] C. Jagadish and S. Pearton (eds.), *Zinc Oxide Bulk, Thin Films and Nanostructures* (Elsevier Science, New York, 2006).

[41] Th. Hahn, *International Tables for Crystallography Volume A: Space-Group Symmetry*, 5th ed. (Springer, Berlin, 2002).

[42] C. Klingshirn, Chem. Phys. Chem. **8**, 782 (2007).

[43] R. R. Birss, *Symmetry and Magnetism* (North-Holland, Amsterdam, 1967).

[44] W. R. L. Lambrecht, A. V. Rodina, S. Limpijumnong, B. Segall, and B. K. Meyer, Phys. Rev. B **65**, 075207 (2002).

[45] R. G. Wheeler and J. Dimmock, Phys. Rev. **125**, 1805 (1965).

[46] J. C. Miklosz and R. G. Wheeler, Phys. Rev. **153**, 913 (1967).

[47] E. L. Ivchenko, in *Excitons*, edited by E. I. Rashba and M. D. Sturge (North-Holland, Amsterdam, 1982).

[48] J. Wrzesinski and D. Fröhlich, Phys. Rev. B **56**, 13087 (1997).

[49] C. Klingshirn, *Semiconductor Optics*, 2nd ed. (Springer, Berlin, 2001).

[50] S. V. Popov, P. Svirko, and N. I. Zheludev, *Susceptibility Tensors for Nonlinear Optics* (Institute of Physics, London, 1995).

[51] P. Guyot-Sionnest and Y. R. Shen, Phys. Rev. B **38**, 7985 (1988).

[52] M. Fiebig, D. Fröhlich, and Ch. Pahlke-Lerch, Phys. Status Solidi B **177**, 187 (1993).

[53] M. Cobet, Ch. Cobet, M. R. Wagner, N. Esser, Ch. Thomsen, and A. Hoffmann, Appl. Phys. Lett. **96**, 031904 (2010).

[54] Previous publications 48 and 52 point out that 1s excitons of the A and B series cannot be treated separately. Considering their coupling leads to the formation of three polariton branches, whereas the middle polariton branch is determined by $1s_{\mathrm{L}}(A,\Gamma_5)$ for small k and $1s_{\mathrm{T}}(B,\Gamma_5)$ for large k, instead of two polariton branches for each series.

[55] R. Dinges, D. Fröhlich, B. Staginnus, and W. Staude, Phys. Rev. Lett. **25**, 922 (1970).

[56] M. Fiebig, Ph.D. thesis, Dortmund University, Germany, 1992.

[57] J. E. Sipe, D. J. Moss, and H. M. van Driel, Phys. Rev. B **35**, 1129 (1987).

[58] J. L. P. Hughes and J. E. Sipe, Phys. Rev. B **53**, 10751 (1996).

[59] J. E. Sipe and E. Ghahramani, Phys. Rev. B **48**, 11705 (1993).

[60] J. E. Sipe and A. I. Shkrebtii, Phys. Rev. B **61**, 5337 (2000).

[61] D. J. Moss, E. Ghahramani, J. E. Sipe, and H. M. van Driel, Phys. Rev. B **41**, 1542 (1990).

[62] D. J. Moss, J. E. Sipe, and H. M. van Driel, Phys. Rev. B **36**, 9708 (1987).

[63] C. Aversa and J. E. Sipe, Phys. Rev. B **52**, 14636 (1995).

[64] S. N. Rashkeev, W. R. L. Lambrecht, and B. Segall, Phys. Rev. B **57**, 3905 (1998).

[65] S. N. Rashkeev and W. R. L. Lambrecht, Phys. Rev. B **63**, 165212 (2001).

[66] S. N. Rashkeev, S. Limpijumnong, and W. R. L. Lambrecht, Phys. Rev. B **59**, 2737 (1999).

[67] S. N. Rashkeev, W. R. L. Lambrecht, and B. Segall, Phys. Rev. B **57**, 9705 (1998).

[68] D. Park, *Introduction to the Quantum Theory* (McGraw-Hill, New York, 1974).

[69] R. J. Elliot, Phys. Rev. **108**, 1384 (1957).

[70] R. D. R. Bhat, P. Nemec, Y. Kerachian, H. M. van Driel, J. E. Sipe, and A. L. Smirl, Phys. Rev. B **71**, 035209 (2005).

[71] L. E. Golub and E. L. Ivchenko, JETP **112**, 152 (2011).

[72] A. G. Samoilovich and L. L. Korenblit, Dokl. Akad. Nauk SSSR **100**, 43 (1955).

[73] D. G. Thomas and J. J. Hopfield, Phys. Rev. Lett. **5**, 505 (1960).

[74] D. Thomas and J. Hopfield, Phys. Rev. **124**, 657 (1961).

[75] E. F. Gross, B. P. Zakharchenya, and O. V. Konstantinov, Fiz. Tverd. Tela (Leningrad) **3**, 305 (1961) [Sov. Phys. Solid State **3**, 221 (1961)].

[76] M. Lafrentz, D. Brunne, B. Kaminski, V. V. Pavlov, A. V. Rodina, R. V. Pisarev, D. R. Yakovlev, A. Bakin, and M. Bayer, Phys. Rev. Lett. **110**, 116402 (2013).

[77] H. Yoshikawa and S. Adachi, Jpn. J. Appl. Phys. **36**, 6237 (1997).

[78] M. R. Wagner, G. Callsen, J. S. Reparaz, R. Kirste, A. Hoffmann, A. V. Rodina, A. Schleife, F. Bechstedt, and M. R. Phillips, arXiv:1312.0529 [Phys. Rev. B (to be published)].

[79] W. L. Bond, J. Appl. Phys. **36**, 1674 (1965).